UCLouvain

AGRO LOUVAIN

Faculté des bioingénieurs

Detecting river ice breakup in small Arctic rivers: combining field data with Sentinel-1 and Sentinel-2 satellite imagery

Case study in the Yukon basin, Alaska

Auteur : Julien EVRARD

Promoteurs : Pr. Sophie OPFERGELT & Baptiste DELHEZ

Lecteurs : Pr. Patrick BOGAERT & Pr. Sophie BONTEMPS

Année académique 2024-2025

Mémoire de fin d'études présenté en vue de l'obtention du diplôme de Bioingénieur : Sciences et technologies de l'environnement

Acknowledgements

Tout d'abord, j'aimerai annoncer un immense merci à ma promotrice Sophie Opfergelt de m'avoir accepté comme mémorant, malgré ma requête tardive. Je vous remercie pour votre gentillesse, vos précieux conseils et votre soutien sans faille tout le long du mémoire. Je ne vous remercierai jamais assez de tout le temps consacré à m'aider et m'aiguiller sur ce mémoire. J'aimerai également remercier tout particulièrement Baptiste Delhez, qui m'a gentiment accordé beaucoup de son temps pour les questions en matière de géomatique, ainsi que pour ses nombreux conseils. Merci également à Maxime Thomas pour avoir aidé pour la relecture de ce mémoire, et pour ses commentaires avisés.

Ensuite, je tiens également à remercier les lecteurs de cette thèse, Sophie Bontemps et Patrick Bogaert, d'avoir accepté de consacrer de leur temps et leur expertise pour la relecture de ce travail.

Enfin, comment ne pas dire merci à ma famille, à Léa, et à Clara, d'avoir pu toujours compter sur eux pendant ces longues années d'études. Merci à vous pour votre présence, et pour votre soutien moral. Après 9 ans, voici enfin le bout du tunnel. Merci !

Table of contents

Acknowledgements **1**

Table of contents **2**

List of figures **4**

List of tables **7**

List of abbreviations ..... Error! Bookmark not defined.

1. Introduction **8**

2. Literature review **9**

2.1. River Ice Processes 9

2.1.1. River ice breakup 10

2.1.2. Climate change and ice dynamics 11

2.1.3. River size influence on monitoring 13

2.2. Remote sensing 13

2.2.1. Remote Sensing Resolutions and Acquisition Modes 14

2.2.2. High-resolution imagery 16

2.2.3. Very High-Resolution Imagery 17

2.2.4. Classification methods 17

3. Objectives **20**

4. Study area **22**

4.1. Panguingue Creek ROI 23

4.2. Nenana ROI 23

4.3. Tanana ROI 24

4.4. Climate 25

5. Materials and methods **27**

5.1. Data collection 27

5.1.1. *In situ* data 27

5.1.2. Satellite data 29

5.2. Spectral indices 33

5.3. Sentinel-2 mapping of river ice cover 35

5.3.1. Pre-processing 35

5.3.2. Processing 37

5.4. Sentinel-1 backscatter change detection 38

5.4.1. Pre-processing 38

5.4.2. Processing 39
6. Results 40
6.1. Temporal resolution 40
6.1.1. Satellite imagery 40
6.1.2. In situ data 43
6.2. Spatial resolution 45
6.2.1. Spectral analysis – Sentinel-2 Random Forest Classification 45
6.2.2. Visual analysis 51
6.2.3. SAR analysis – Sentinel-1 52
7. Discussion 55
7.1. How the temporal resolution of satellite observation affects the detection of river ice breakup 55
7.2. Minimum river width for which ice breakup can be reliably detected based on the spatial resolution analysis 56
7.2.1. Sentinel-2 Random Forest classification 56
7.2.2. Sentinel-1 backscatter difference 58
7.3. Cross-combination of data from satellite imagery with field observations for in situ validation of ice breakup difficult due to data scarcity 58
7.4. Methodological uncertainties and limitations 60
7.4.1. Sentinel-2 Random Forest classification 60
7.4.2. Sentinel-1 backscatter differences 61
8. Conclusion 62
Bibliography 64

List of figures

Figure 1: Discharge data from Kyusyur station from 1936 to 2018. Colours from blue to red indicate the year from 1936 to 2018. The thick solid red line shows the year 2018 and the black thick dashed shows the mean of the period from 1936 to 2018. The inset figure shows the discharge flux for the whole year (green) and for November to April (blue). Discharge data: A.I. Shiklomanov (2010) 1939–2008, ArcticGRO 2009–2019. Extracted from Juhls et al. (2020)... 10

Figure 2: Spatial distribution of projected change in Northern Hemisphere river ice duration under the RCP4.5 emission scenario by 2080–2100 relative to the period 2009–2029. White areas refer to rivers without ice cover in the period 2009–2029 (zero days). Reference period isolines indicate river ice duration in the period 2009–2029. Coloured areas depict loss of ice duration in days. Blue areas depict a projected increase in river ice duration. Grey land areas indicate a lack of Landsat-observable rivers (Data source: Yang et al., 2020). Extracted from IPCC (2023). 12

Figure 3: Pixel resolution and image display. The more pixels an image has, the more detailed it is (Setyawan, n.d.). 14

Figure 4: Frequencies along the electromagnetic spectrum. Optical imagery centres around visible light, near-infrared, and short-wave infrared. SAR utilises bands at the centimetre to metre level. The C-band is the main used band (global mapping, change change detection, monitoring of areas with low to moderate penetration, higher coherence); ice, ocean, maritime navigation (NASA, 2021b)..... 15

Figure 5: Sentinel-1 constellation repeat and coverage frequency across the globe (ESA, 2025). 16

Figure 6: Steps of the Random Forest regression model. The algorithm first builds n decision trees estimators, then averages the predictions of all estimators (*The Ultimate Guide to Random Forest Regression*, 2020)..... 19

Figure 7: General locations of the three study's ROIs in the Yukon River basin: (1) Panguingue Creek ROI, (2) Nenana ROI and (3) Tanana rOI. Only the relevant rivers are shown for clarity purposes. 22

Figure 8: Delimitations, rivers and subwatersheds of the Panguingue Creek ROI. 23

Figure 9: Delimitations, rivers and subwatersheds of the Nenana ROI. 24

Figure 10: Delimitations, rivers and subwatersheds of the Tanana ROI..... 24

Figure 11: Average temperatures, total precipitation and snowfall in Fairbanks for 1991-2020. (Source: Alaska Climate Research Center, n.d.-a)..... 25

Figure 12: River break-up dates on the Tanana River at Nenana as recorded by the Nenana Ice Classic since 1917 until 2024. Average break-up dates for the climate reference periods 1931-1960, 1961-1990 and 1991-2020 are plotted as colored lines for reference. (Source: Alaska Climate Research Center; data from nsidc.org, nenanaakicceclassic.com)..... 26

Figure 13: Evolution of river ice cover on Panguingue Creek in 2018 (Credit: Opfergelt et al.). 27

Figure 14: The Nenana Ice Classic tripod. Photo taken on March 24, 2009 (Credit: James Brooks)..... 28

Figure 15: Changes in backscatter signal due to the difference between ascending and descending orbit (Bouvet et al., 2018)..... 30

Figure 16: Sentinel-2 L2A pre-processing workflow, done in QGIS Python Console Plugin 36

Figure 17: Stratified random sampling design (AcATaMa, n.d) 37

Figure 18: Before and after SCL cloud mask was applied on Sentinel-2 imagery for the ROI of Panguingue Creek. A.1) and A.2) show the result on the B12 band for the 05/05, while B.1) and B.2) show the result on the B12 band for the 13/05. Based on the coverage of the SCL cloud mask, 13/05 was removed from the data pool..... 41

Figure 19: Sentinel-1, Sentinel-2 and PlanetScope data availability during the 2018 thawing season (April to May) for the different ROIs. For Sentinel-2, the data available passed the SCL test. Breakup dates for each ROI is highlighted in red. A) Panguingue Creek ROI; B) Nenana ROI; C) Tanana ROI. 42

Figure 20: Daily mean air temperature (°C) and breakup dates for each ROI, and daily mean discharge (m^3/s) for Nenana ROI. A) Panguingue Creek ROI; B) Nenana ROI ; C) Tanana ROI. Mean discharge is directly measured from station data. Estimated mean discharge is based on expert judgement (USGS, 2019, 2024). Data ranging from April 1 2018 to June 10 2018. (Source: Alaska Climate Research Center (https://akclimate.org)) 43

Figure 21: Temporal series of Panguingue Creek ROI's land cover, based on Random Forest classifications of Sentinel-2 data. A) 16/04; B) 25/04; C) 05/05; D) 28/05. 46

Figure 22: Temporal series of Nenana ROI's land cover, based on Random Forest classifications of Sentinel-2 data. A) 16/04; B) 25/04; C) 05/05; D) 28/05. 48

Figure 23: Targeted analysis of two areas within the Panguingue Creek ROI to qualitatively assess river detection, with indicative river presence provided to support visual interpretation. Images A were acquired on 05 May, and images B on 28 May. (A.1, B.1) Random Forest classification from Sentinel-2; (A.2, B.2) Sentinel-2 imagery. (Source: Sentinel-2, Copernicus Browser; Gerad Smith). 50

Figure 24: Targeted analysis of two areas within the Nenana ROI qualitatively assess river detection, with indicative river presence provided to support visual interpretation. Images A were acquired on 25 April, and images B on 05 May. (A.1, B.1) Random Forest classification from Sentinel-2; (A.2, B.2) Sentinel-2 imagery. (Source: Sentinel-2, Copernicus Browser; Gerad Smith). 51

Figure 25: Absolute and relative differences in Sentinel-1 backscattering between three sets of dates at the Nenana ROI. A) 24-22 April B) 4 May-24 April C) 18-6 May. (A.1, B.1, C.1) Absolute difference in backscattering; (A.2, B.2, C.2) Relative difference in backscattering. Maximum and minimum values differ slightly for each date; therefore, no units were added in the legend. (Source: Sentinel-1 GRD IW VV band, Copernicus Browser). 53

Figure 26: Absolute and relative differences in Sentinel-1 backscattering between 18 May and 06 May at the Panguingue Creek ROI. A) Absolute difference; B) Relative difference. Maximum and minimum values differ slightly for each date; therefore, no units were added in the legend. (Source: Sentinel-1 GRD IW VV band, Copernicus Browser). 54

Figure 27: Comparison of mean river discharge (m^3/s) of the Tanana River at the Nenana ROI in 2009 and 2018. Mean discharge is directly measured from station USGS-15515500 data. Estimated mean discharge is based on expert judgement (USGS, 2019, 2024). Coincidentally, breakup is occurring on the same day, May 1. (Sources: NOAA, n.d.; USGS, n.d.). 59

Figure 28: Exemples of errors in the cloud screening preprocessing for the Panguingue Creek ROI on April 25. A) SWIR; B) True Color; C) RF classification. 61

List of tables

Table 1: Sentinel-1 C-SAR bands polarisation and spatial resolution 30

Table 2: Spectral resolution of the Sentinel-2 bands used for this study 32

Table 3: Spectral resolution of the PlanetScope data used for this study 33

Table 4: Summary of each spectral index or composite, its primary highlight, and the bands or formula used. 34

Table 5: Key results of Panguingue Creek Random Forest classifications (16/04; 25/04; 05/05; 28/05): overall, producer, and user accuracies of the classes of interest (Water, Snow, Melting snow, and Ice), where n= number of samples. 47

Table 6: Key results of Nenana Random Forest classifications (16/04; 25/04; 05/05; 28/05). Here are represented the overall, producer, and user accuracies of the classes of interest (Water, Snow, Melting snow, and Ice), where n= number of samples. 49

1. Introduction

Over half of the Northern Hemisphere's river network is seasonally ice-covered, draining more than one-third of Earth's landmass (Bennett & Prowse, 2010). Ice cover regulates winter hydrology, sediment transport, and provides habitat for numerous species (e.g., Beltaos & Burrell, 2003; Thellman et al., 2021). Climate change is driving later freeze-up, earlier breakup, and a shortening of the ice season by more than two weeks annually (Adrian et al., 2009; Sharma et al., 2019). These shifts, amplified in Arctic regions due to polar affect ecosystems, infrastructure, and local communities warming (AMAP, 2021; Rantanen et al., 2022).

Monitoring river ice breakup remains difficult in remote terrain, particularly for small rivers where observational records are sparse (Thellman et al., 2021). Remote sensing provides a consistent and cost-effective means to assess ice phenology over large and inaccessible areas (Yang et al., 2020). Advances in open-access satellite imagery, such as the Sentinel missions, now allow detailed time-series analyses that were previously restricted to wide rivers. However, small channels remain understudied despite their ecological significance and high variability in ice processes (Turcotte et al., 2014; Vonk et al., 2023). Improved monitoring of these systems is necessary to capture local dynamics, refine predictive models, and better understand the impacts of climate change on Arctic river networks.

This study aims to determine what is the minimum river width at which river ice breakup can be detected in the Arctic using open-access satellite imagery. Three objectives guide the work. First, assess how temporal resolution affects the ability to identify breakup dates or narrow the uncertainty window. Second, evaluate how spatial resolution limits detection by defining the minimum observable river width. Third, integrate satellite data with in situ records of air temperature, discharge, ice thickness, and breakup timing to provide complementary information.

The study analyses three regions of interest in central Alaska, near Healy, Nenana, and Tanana, covering rivers of different sizes during the breakup season (April-May 2018). Two approaches using open-access satellite imagery are developed: Sentinel-1 backscatter change detection and the classification of Sentinel-2 optical time series with a Random Forest algorithm to distinguish snow, ice, and open water. PlanetScope imagery and spectral indices provide high-resolution reference data to confirm classification accuracy and spatial detectability.

2. Literature review

Over half of the Northern Hemisphere's river network is seasonally ice-covered, draining more than a third of Earth's landmass (Bennett & Prowse, 2010). Ice cover regulates winter hydrology, sediment transport, and provides habitat for aquatic and riparian species (e.g., Beltaos & Burrell, 2003; Thellman et al., 2021). However, climate change and human activity are rapidly altering river ice phenology, with cascading impacts on ecosystems and communities (Yang et al., 2020).

2.1. River Ice Processes

River ice evolves through three seasonal phases. During the freeze-up period (October to January), ice begins to form as frazil and border ice develops under cooling atmospheric and water conditions. In mid-winter (January to March), the ice cover thickens through congelation and is influenced by snow accumulation and changes in river discharge. The breakup phase (April to May) occurs when the ice cover deteriorates due to rising temperatures or increased river flow, which can result in either gradual melting or dynamic fracturing and displacement. This period is also marked by a surge in river discharge as melting ice and snowpack contribute to additional flow, often intensifying the breakup process (Figure 1). Arctic warming has led to thinner ice and earlier breakups (Magnuson et al., 2000; Lesack et al., 2014).

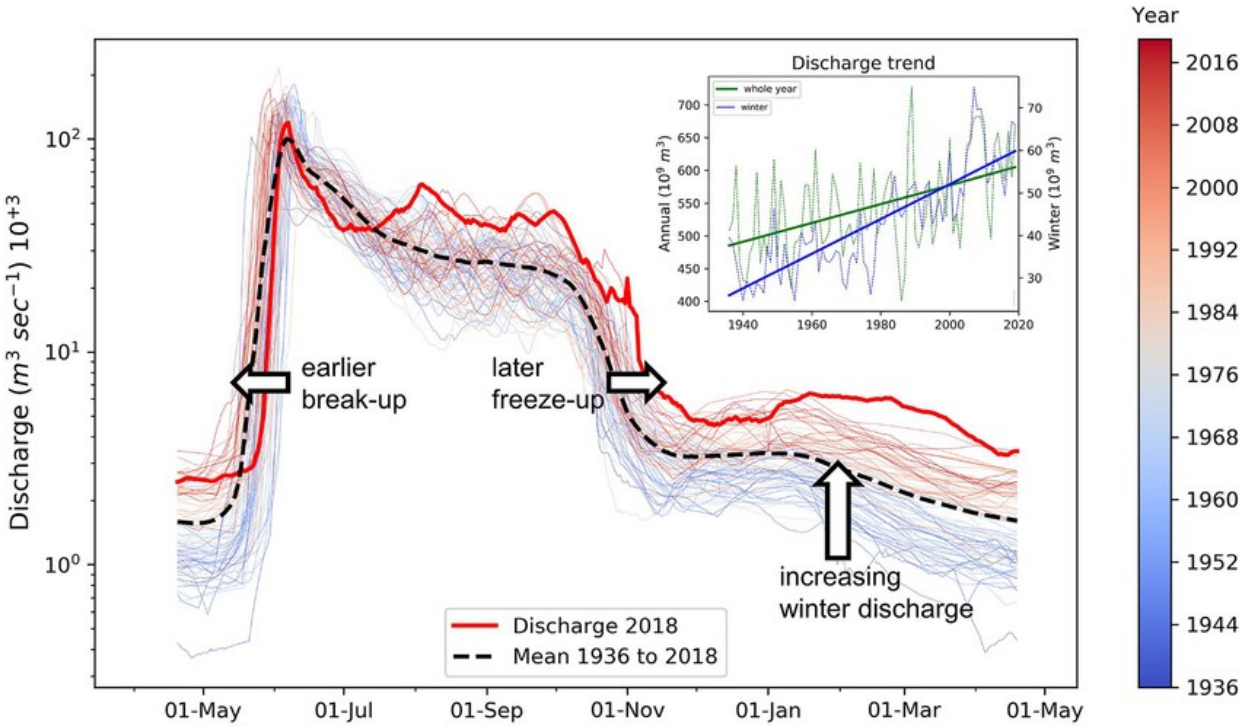


Figure 1: Discharge data from Kyusyur station from 1936 to 2018. Colours from blue to red indicate the year from 1936 to 2018. The thick solid red line shows the year 2018 and the black thick dashed shows the mean of the period from 1936 to 2018. The inset figure shows the discharge flux for the whole year (green) and for November to April (blue). Discharge data: A.I. Shiklomanov (2010) 1939–2008, ArcticGRO 2009–2019. Extracted from Juhls et al. (2020).

2.1.1. River ice breakup

Breakup is governed by ice type and unlike freeze-up, they are more strongly influenced by climatic (rather than geomorphic) conditions (Thellman et al., 2021).

River ice breakup generally falls into two categories: mechanical (or dynamic) and thermal. Mechanical breakup follows a period of cold early spring temperatures and rapid warming, often intensified by thick ice and high snowpack in the headwaters. This type typically drives ice downstream in a linear pattern and is more likely to produce ice jams and flooding. In contrast, thermal breakup occurs under gradually warming temperatures, causing the ice to deteriorate and melt in place, with fewer and less severe jams. Most breakups are a combination of these two types (Beltaos & Prowse, 2009).

Breakup dynamics are highly site-specific, even among low-order streams within the same watershed. A study of breakup dynamics in the lower Montgomery River watershed in 2014 illustrates how ice behaviour varies across channels of different sizes (Turcotte et al., 2014; Thellman et al., 2021). In the smallest stream (1 to 2 m wide), no mechanical breakup occurred because any winter ice cover had already weakened or vanished due to sustained groundwater

inflow prior to the spring freshet. In slightly wider channels (3 to 4 m), both surface and border ice formed. During breakup, surface ice detached first, while border ice persisted for several hours before slowly melting under rising discharge. In the largest studied channel (15 to 20 m), surface and bottom ice dislodged nearly simultaneously when increased flow submerged large in-channel boulders. Here, weaker lateral integration with the banks made the ice more mobile and prone to early release (Turcotte et al., 2014).

Inconsistencies in observational records and differing definitions of break-up undermine the comparability of river ice research across regions and time. One study may define breakup as the first visible crack or motion in the ice, another may use the first observation of open water, while yet another considers complete ice clearance as the threshold (Prowse et al., 2007). These definitional discrepancies introduce bias and uncertainty into trend assessments, complicating inter-site comparisons and meta-analyses in river-ice science.

2.1.2. Climate change and ice dynamics

Observed ice loss

River ice forms later and melts earlier than in previous decades, shortening the ice season by more than two weeks annually (Adrian et al., 2009; Sharma et al., 2019). Between 1984 and 2018, global river ice extent declined by 25% (Yang et al., 2020). These changes are especially pronounced at high latitudes due to polar amplification, a phenomenon causing the Arctic to warm up to four times faster than the rest of the globe (Du et al., 2017; AMAP, 2021; Rantanen et al., 2022). High-confidence evidence links these trends to climate change based on long-term observational and remote sensing data (Figure 2).

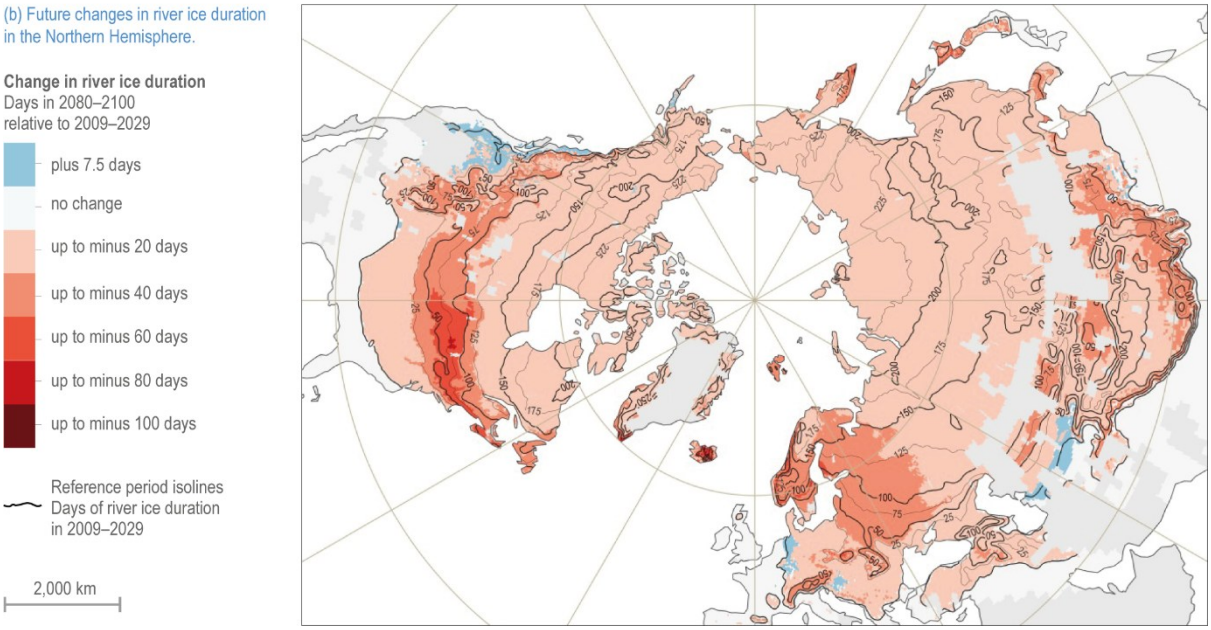


Figure 2: Spatial distribution of projected change in Northern Hemisphere river ice duration under the RCP4.5 emission scenario by 2080–2100 relative to the period 2009–2029. White areas refer to rivers without ice cover in the period 2009–2029 (zero days). Reference period isolines indicate river ice duration in the period 2009–2029. Coloured areas depict loss of ice duration in days. Blue areas depict a projected increase in river ice duration. Grey land areas indicate a lack of Landsat-observable rivers (Data source: Yang et al., 2020). Extracted from IPCC (2023).

Variation in ice formation and dynamics

Ice cover varies with river size, morphology, and regional conditions (Turcotte & Morse, 2013). Larger rivers, with higher thermal inertia, are more influenced by temperature, while smaller rivers are shaped additionally by vegetation, snow, groundwater, flow velocity, and topography (Lind et al., 2016).

Small rivers host a wider variety of ice types due to variable morphology and groundwater input (Turcotte et al., 2014). Surface water-groundwater interactions, not necessarily predictable with river size, further complicate ice dynamics (Thellman et al., 2021). Furthermore, the sequence and type of weather events also matter. For instance, rain falling on snow followed by a drop in temperature can enhance ice formation by creating slush that freezes, while persistent early snowfall can insulate the river surface and inhibit ice growth, even when surface air temperatures remain low (Prowse et al., 2007; Turcotte & Morse, 2017).

Climate change is altering the ice thickness, type, and seasonality. While mechanical breakups may increase with abrupt melt events, warmer winters favour thinner ice and more thermal breakups (Bennett & Prowse, 2010; Lindsey, 2019). The ecological implications include altered nutrient flows, floodplain connectivity, and instream productivity (Thellman et al., 2021). Ice more frequently interacts with the substrate in small, shallow, groundwater-limited rivers,

where it may freeze completely or form anchor ice. In contrast, ice typically forms as surface cover above the aquatic community in larger rivers (Turcotte & Morse, 2013). Therefore, ice exerts more direct physical effects on biota in small to medium rivers.

Ice timing and duration are shifting in response to warmer winters (Magnuson et al., 2000; Bennett & Prowse, 2010). However, responses vary by river size. Smaller, steep headwater streams may experience colder winter water temperatures due to reduced insulation, while larger rivers may warm due to broader climatic influences (Turcotte & Morse, 2017).

The timing of winter ice conditions is projected to vary as winter temperatures increase and this aspect of winter climate change poses the greatest uncertainty in a river's ecological response.

Future studies should quantify ice dynamics across diverse river sizes and climates, particularly in small, understudied systems (Vonk et al., 2023). Due to monitoring challenges, trends in headwater ice dynamics remain largely undocumented (Thellman et al., 2021). Empirical data are essential for developing models that reflect real-world variability in hydrology, morphology, and climate.

2.1.3. River size influence on monitoring

Research and monitoring have focused on large rivers due to several factors. First, ice breakup-related ice jams and floods cause a massive $300 million infrastructure damage each year in North America (Morales-Marín et al., 2019). Furthermore, large rivers play an important role for transportation, hunting, and fishing, in remote Arctic areas with minimal or non-existent road access (Dong et al., 2025). Finally, remote sensing technologies are more effective on wide rivers, leaving small streams understudied (Thellman et al., 2021; Yang et al., 2020). Recent high-resolution satellites and *in situ* tools offer new opportunities for studying ice in smaller channels. An overview of how remote sensing approaches can be applied to monitor river ice processes is provided in the next section.

2.2. Remote sensing

Remote sensing is the science of acquiring information about Earth's surface without direct contact, typically using instruments aboard satellites or aircrafts. These instruments detect and measure reflected or emitted electromagnetic energy, offering a global, repeatable, and cost-effective means of monitoring environmental phenomena. For river ice cover, remote sensing provides consistent observations across vast and often inaccessible areas, essential for understanding ice dynamics, safety, and hydrological implications.

2.2.1. Remote Sensing Resolutions and Acquisition Modes

Satellite imagery quality and usability depend on four key resolution types.

Spatial resolution refers to the size of the smallest feature that can be identified by a satellite sensor or displayed in a satellite image (Figure 3). It defines the ground area represented by a single pixel; higher spatial resolution (e.g., 10 m) allows detection of finer features, such as narrow ice-covered rivers (*Satellite Applications for Geoscience Education*, n.d.).

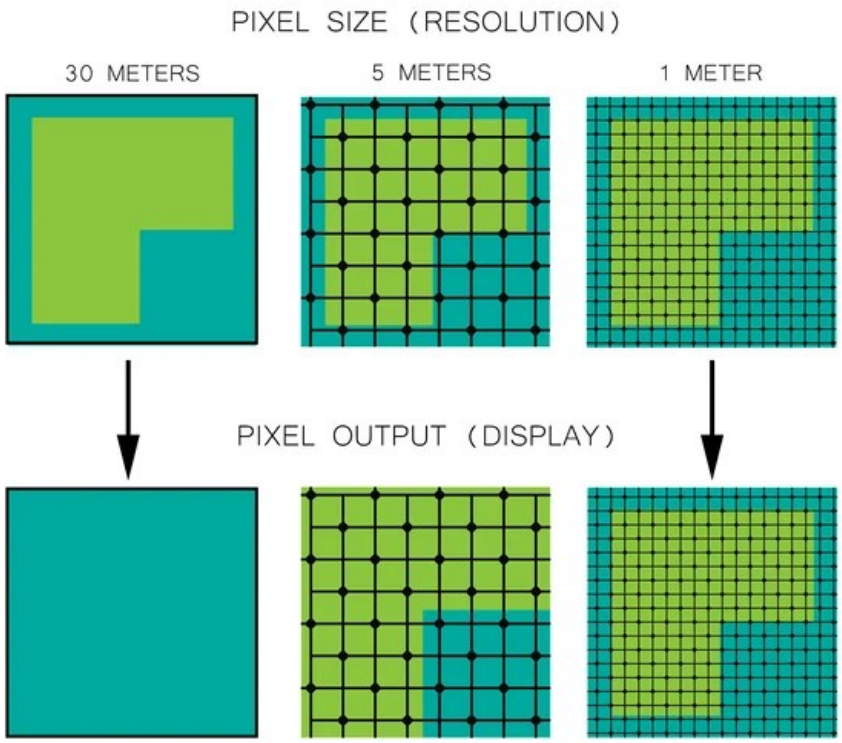


Figure 3: Pixel resolution and image display. The more pixels an image has, the more detailed it is (Setyawan, n.d.).

Temporal resolution refers to how frequently a satellite revisits the same location; high temporal resolution (e.g., daily or every few days) is crucial for tracking dynamic events like ice breakup.

Spectral resolution describes the number and width of spectral bands a sensor can detect, with multispectral instruments improving material differentiation, such as distinguishing ice from water or snow.

Radiometric resolution indicates the sensitivity of a sensor to detect slight differences in energy, enabling finer discrimination of surface characteristics to assess subtle ice conditions.

Achieving high resolution across all four categories of resolution is technically demanding and often requires trade-offs, for example between spatial detail and revisit frequency.

In terms of acquisition modes, optical sensors are passive instruments that capture solar-reflected radiation in visible, near-infrared (NIR), and short-wave infrared (SWIR) bands.

However, they rely on daylight and clear skies, which limits their usefulness during cloud cover or polar night.

Synthetic Aperture Radar (SAR), on the other hand, is an active system that emits microwave signals and records backscattered responses, functioning regardless of weather or light conditions and making it ideal for monitoring river ice (Figure 4).

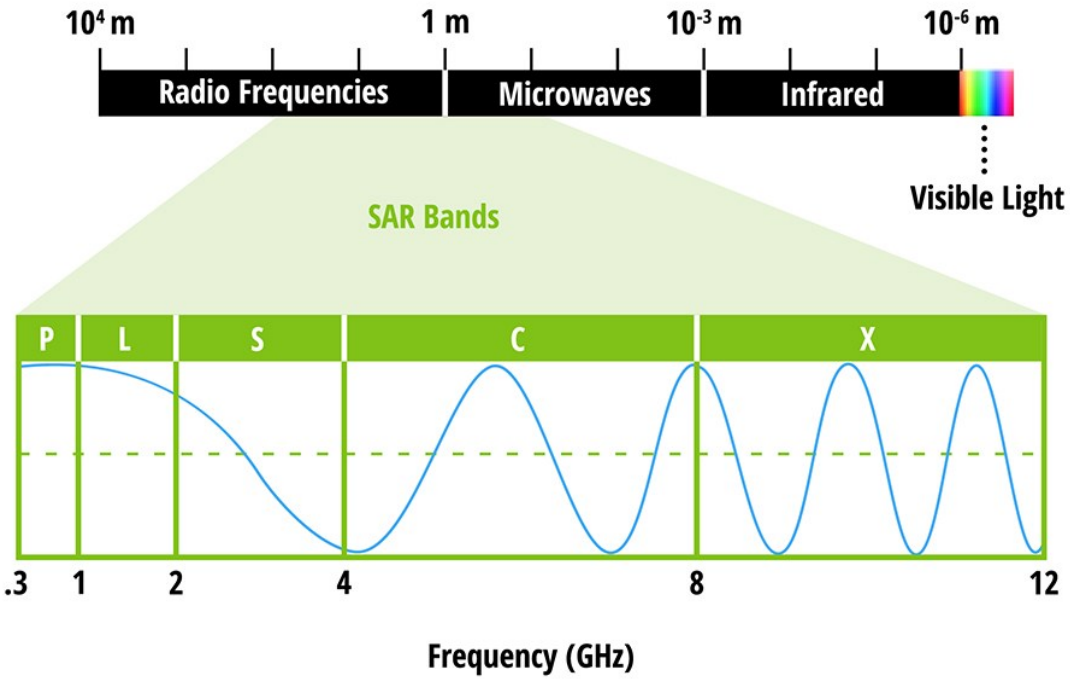


Figure 4: Frequencies along the electromagnetic spectrum. Optical imagery centres around visible light, near-infrared, and short-wave infrared. SAR utilises bands at the centimetre to metre level. The C-band is the main used band (global mapping, change change detection, monitoring of areas with low to moderate penetration, higher coherence); ice, ocean, maritime navigation (NASA, 2021b)

LiDAR, another active method, uses laser pulses to create detailed 3D models of Earth's surface. Although not common on satellites, airborne LiDAR is effective for topographic mapping, elevation modelling, and floodplain analysis. However, limited spatial coverage (swath widths less than 1 km) and high costs restrict its use to targeted studies rather than basin-scale monitoring (Agrawal & Khairnar, 2019).

2.2.2. High-resolution imagery

Copernicus is the European Union's Earth Observation Programme, providing information services based on satellite (the Sentinel families) and *in situ* data. It collects and transforms data from various sources, including satellites and ground-based sensors. The programme offers free open access high-resolution imagery. Launched between 2014 and 2017, Sentinel's data archive facilitates time-series analyses, which are crucial for long-term river ice studies.

Sentinel-1 (SAR)

Sentinel-1 comprises two polar-orbiting satellites equipped with C-band SAR sensors, launched in 2014 and 2016. The primary land mode is Interferometric Wide (IW) swath with a spatial resolution of 20 m and each satellite has a revisit time of 12 days (Figure 5). Sentinel-1 delivers dual-polarisation data, critical for ice type discrimination and classification. It supports continuous, all-weather monitoring and is particularly effective in high-latitude regions and during cloudy or dark conditions. Dual polarisation (VH and VV) is a standard for operational ice classification: cross-polarisation (e.g. VH) is more sensitive than co-polarisation (e.g. VV).

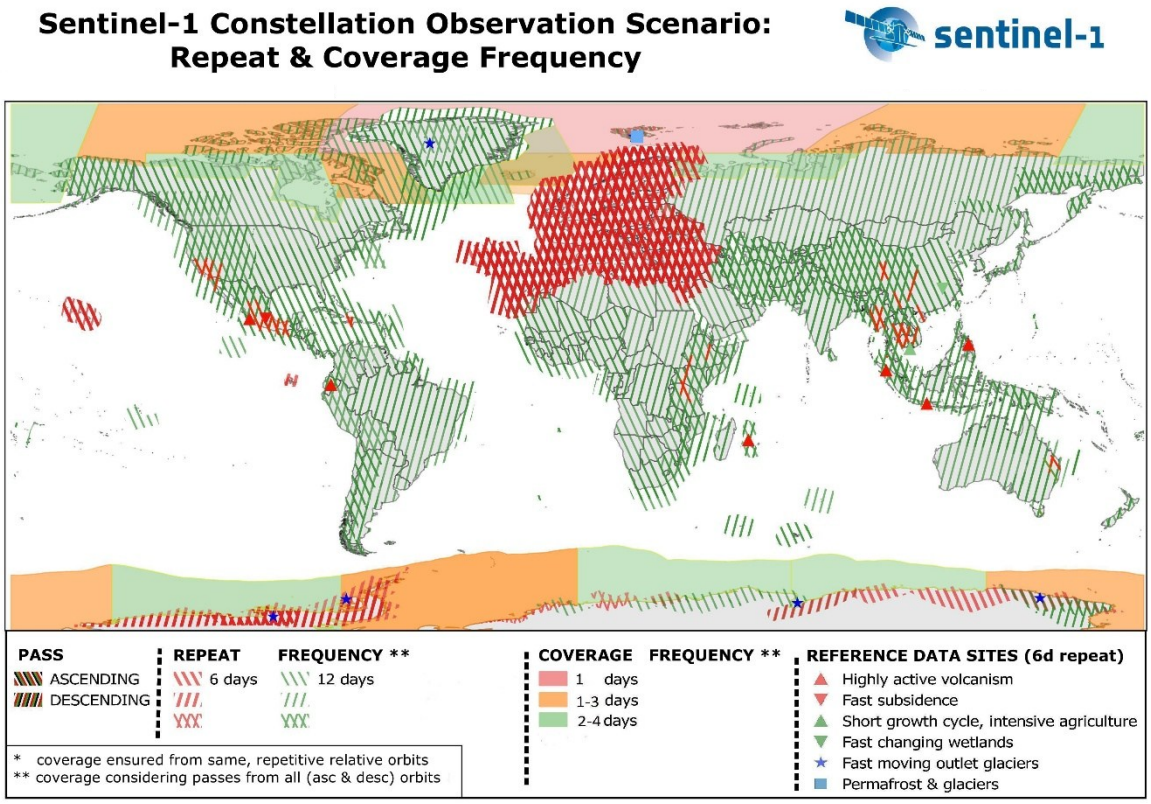


Figure 5: Sentinel-1 constellation repeat and coverage frequency across the globe (ESA, 2025).

Sentinel-2 (Optical)

Sentinel-2 offers high-resolution (10 to 60 m) multispectral imagery across 13 bands, with a revisit time of 5 days at mid to high latitudes; even less than five days at latitudes above 60°N (J. Li & Chen, 2020). The mission is comprised of twin satellites launched in 2015 and 2017. It

provides valuable data for mapping ice extent using spectral signals of ground features. However, cloud cover significantly hinders data availability, as clouds interfere with the spectral signals, rendering data unexploitable. It can be particularly impactful on short periods like spring breakup. Its 10 m visible and NIR bands, 20 m SWIR bands, and wide swath (290 km) make it suitable for regional-scale ice monitoring under favourable weather.

2.2.3. Very High-Resolution Imagery

PlanetScope (Optical)

PlanetScope, operated by Planet Labs, consists of a constellation of CubeSats (Dove satellites) delivering very high-resolution imagery (3.7 m, resampled at 3 m) with near-daily global coverage. Original Dove constellation design consists of Red, Green, Blue and Near-Infrared spectral bands. This capability supports precise ice edge detection in rivers as narrow as 10 m. The trade-offs include limited radiometric calibration (around ± 12% uncertainty) and higher costs compared to free data from Copernicus missions (Rösch et al., 2022). Accessing PlanetScope data is free for students and faculties through the Education and Research programme, but limited to 3,000 km² per month (Planet, 2025). Despite this, PlanetScope's high spatial and temporal resolution makes it a valuable tool for targeted river ice monitoring where detail and frequency are crucial.

2.2.4. Classification methods

Image classification algorithms can help better discriminate different land cover types. Classification relies on features whose pixel values indicate specific classes. These features are often spectral reflectance values, but can also include water and ice indices, texture measures, or other derived metrics depending on the application. Ice cover studies can employ spectral indices such as the Normalised Difference Snow Index (NDSI) or ice texture to differentiate between solid and frazil ice. A program using image classification algorithms can automatically categorize pixels through a process referred to as unsupervised classification. In supervised classification, the user provides reference areas of known land cover types to train the algorithm to categorize similar pixels. Additionally, classified imagery can be integrated into a Geographic Information System (GIS), enabling the comparison of each pixel with supplementary spatial data.

In addition to selecting appropriate satellite data, the choice of classification method is critical and must align with the characteristics of the intended application. For instance, mapping extensive areas with noisy, complex data and limited training samples requires algorithms capable of handling high variability and sparse labelling (e.g., Rodriguez-Galiano et al., 2012).

Methods may also be categorized as parametric or non-parametric, making or not assumptions about the data distribution, and as pixel-based or object-based, grouping pixels into meaningful objects, then classifying those objects rather than individual pixels. Increasingly, machine-learning algorithms (especially non-parametric classifiers) dominate remote sensing applications due to their flexibility and accuracy (Lary et al., 2016; Ma et al., 2019).

Machine Learning Classifiers

Machine learning classifiers such as classification and regression trees (CART), artificial neural networks (ANNs), and support vector machines (SVMs) have proven effective in complex classification tasks. These methods outperform traditional parametric approaches in large, high-dimensional feature spaces (Rodriguez-Galiano et al., 2012; Ma et al., 2019). Their non-parametric nature, strong class boundary modelling, and compatibility with diverse data types enhance their utility (Maxwell et al., 2018).

However, SVMs and ANNs often require extensive parameter tuning and computational resources, limiting scalability. Ensemble methods offer a solution by improving classification robustness and accuracy through aggregation of multiple base classifiers (e.g., Breiman, 2001).

Choosing the optimal machine learning classifier is challenging due to methodological differences across studies and context-specific performance. Comparative studies often yield contradictory results; for example, Rogan et al. (2008) found ANNs more accurate than decision trees, while Lippitt et al. (2008) reported the opposite. Some studies found SVM and Random Forest (RF) equally accurate, while others reported superior performance by SVM (Pal, 2005; Kingma & Ba, 2014; Adam et al., 2014).

A systematic comparison by Lawrence and Moran (2015), using consistent procedures across 30 datasets, found RF to have the highest average accuracy (73.19%), outperforming SVM (62.28%) in most cases. However, RF was the best classifier in only 18 of the 30 datasets, underscoring the influence of data characteristics on performance.

Evidence suggests ensemble methods, particularly those based on decision trees like RF and boosted decision trees, generally offer higher accuracy than single classifiers (Lee, Joonwhoan, 2014). Although SVM ensembles have also been explored, decision trees-based ensembles are preferred for their speed and compatibility with bagging and boosting techniques.

Classifier performance depends not only on algorithm choice but also on training data quality, parameter settings, and feature selection. Thus, users are encouraged to test multiple classifiers and evaluate not only overall accuracy but also class-specific metrics, especially for rare classes. If testing multiple classifiers is not feasible, SVM, RF, and boosted decision trees are reliable options. RF, in particular, combines high accuracy, computational efficiency, resistance to overfitting, and feature ranking capabilities, making it suitable for multi-source remote sensing and geographic data integration. While it may sacrifice interpretability, its robustness and versatility make RF a preferred choice in many applications (Maxwell et al., 2018).

Random Forest

Random Forest, an ensemble method introduced by Breiman (2001), is among the most widely used classifiers in remote sensing (Maxwell et al., 2018). It builds multiple CARTs using bootstrapped training samples and random subsets of predictor variables. Each tree votes for a class, and the majority decision determines the final classification (Figure 6).

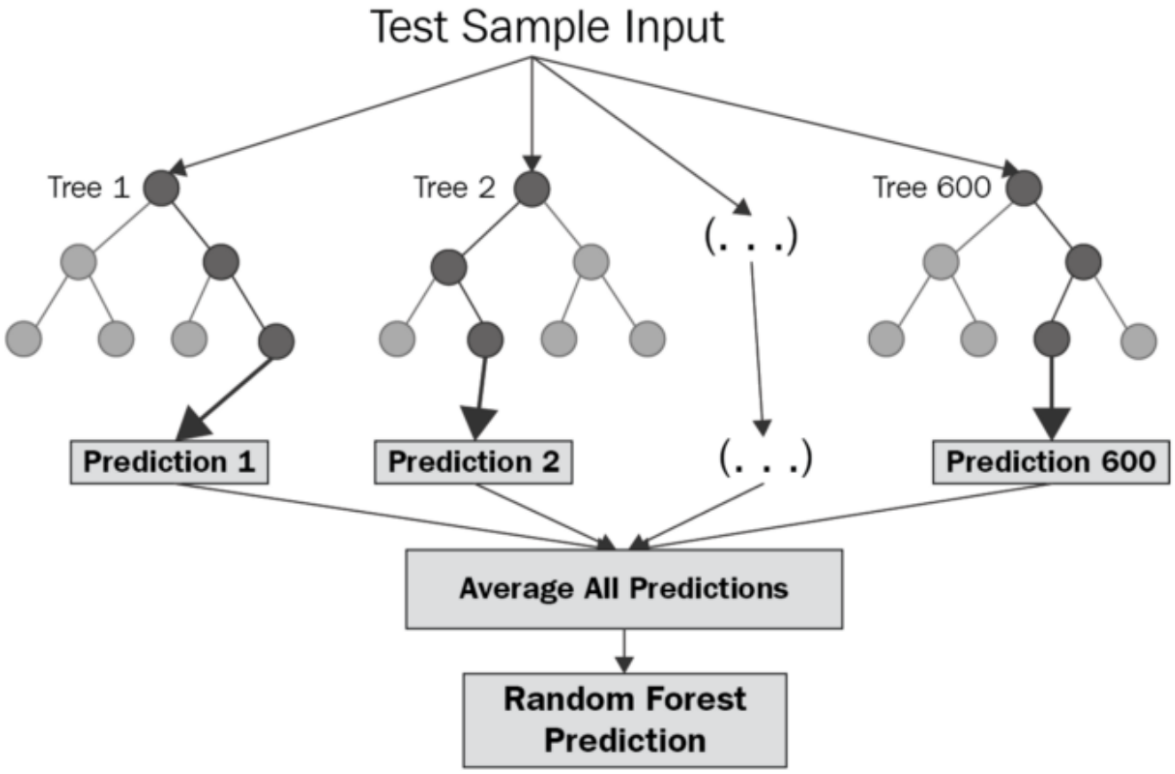


Figure 6: Steps of the Random Forest regression model. The algorithm first builds n decision trees estimators, then averages the predictions of all estimators (*The Ultimate Guide to Random Forest Regression*, 2020).

The strength of RF lies in its low bias and variance stabilization due to tree ensemble diversity. Its advantages include high accuracy, robustness to overfitting and noise, ability to estimate variable importance, and minimal parameter tuning (*IBM Integrated Analytics System*, 2022). Unlike boosting, RF is computationally efficient, making it suitable for large-scale applications.

Despite its strengths, RF is often considered a "black box" model (Fung et al., 2021). Feature importance is assessed at the global classification level, which may overlook locally significant variables. Moreover, while RF typically performs well, it can overfit in specific contexts, and the model structure is not easily interpretable, as a single decision tree is easier to interpret than a forest of them (*What Is Random Forest?*, 2021).

RF has been successfully applied to diverse remote sensing tasks, including land cover classification and ice cover mapping (Lu et al., 2020; Mugunthan et al., 2023). Its internal out-of-bag (OOB) validation and feature importance metrics support model evaluation and refinement.

Spectral indices

Spectral indices are mathematical expressions that combine data from different spectral bands in multispectral or hyperspectral images to highlight features of interest, such as vegetation, water, or built-up areas. They are used in remote sensing to analyse satellite data and derive information about the Earth's surface (Montero et al., 2023).

3. Objectives

The *main objective* of this study is to improve the detection of the ice breakup occurrence for small Arctic rivers. This leads to the following *research question* for this study:

What is the minimum river size where ice break-up is detectable in the Arctic using open access satellite imagery?

To address this research question, this study is subdivided in three *specific objectives,* each associated with a working hypothesis:

1. Evaluate how the temporal resolution of satellite observation affects the detection of river ice breakup. Specifically, determining the precise date of breakup or at least narrow the uncertainty window around it.

> *Working hypothesis:* Smaller rivers experience earlier breakup due to lower thermal inertia.

2. Evaluate how the spatial resolution of satellite observation performs. Specifically, defining the minimum river width for which ice breakup can be reliably detected, given the resolution limits of various satellite sensors.

> *Working hypothesis* based on a general remote sensing principle: to reliably detect a feature, it must be at least twice the size of the sensor's spatial resolution. Thus, narrower rivers may fall below the detectable threshold for high-resolution sensors like Sentinel-2.

3. Cross-combine data from satellite imagery with field observations for in situ validation.

> *Working hypothesis:* River discharge increases immediately after breakup, primarily due to enhanced runoff from melting ice and snow. This pattern has been observed in larger rivers such as the Lena River and may apply more broadly across Arctic rivers.

Our approach is the following:

1. In order to capture the ice breakup, we selected three regions of interest (ROIs) covering a range of Arctic rivers of varying sizes, from large systems to small tributaries. This also enabled the evaluation of the performance of classification methods across different spatial scales, including river junctions and narrow channels.

2. With the aim of narrowing the time window for ice-breakup detection, we combine remote sensing approach (open access satellite imagery) and *in situ* data. Time series of Sentinel-2 and Sentinel-1 data are assembled for each ROI, covering the period leading up to, during, and after the expected breakup window. The objective is to identify the onset of ice breakup with the highest possible temporal accuracy. Where available, *in situ* observations and records of breakup dates are used as reference data to validate remote sensing results, reducing the uncertainty associated with the timing of the breakup.

3. To contribute to improve the spatial resolution by combining different sources of satellite imagery:

- Firstly, assess how snow, ice, and open water can be detected in rivers of different widths by applying Random Forest (RF) classification on a time series of Sentinel-2 data

- Secondly, evaluate how ice breakup can be detected using relative and absolute subtraction approaches to detect changes in backscatter on Sentinel-1 SAR data. This method allowed the identification of surface transitions regardless of cloud cover or light conditions.

- Thirdly, verify classification outputs and spatial detectability using PlanetScope imagery and spectral indices as a high-resolution reference.

4. Study area

The three selected regions of interest (ROIs) are located in Central Alaska, in the United States of America.

They are located at river junctions across the Yukon River basin, starting from Panguingue Creek and the successive river junctions until Yukon River at Tanana. The three selected ROIs are centred around (1) the river junction between Panguingue Creek and Nenana River north the locality of Healy (called Panguingue Creek ROI), (2) the river junction between Nenana River and Tanana River at the city of Nenana (called Nenana ROI) and (3) the river junction between Tanana River and Yukon River at the city of Tanana (called Tanana ROI) (Figure 7).

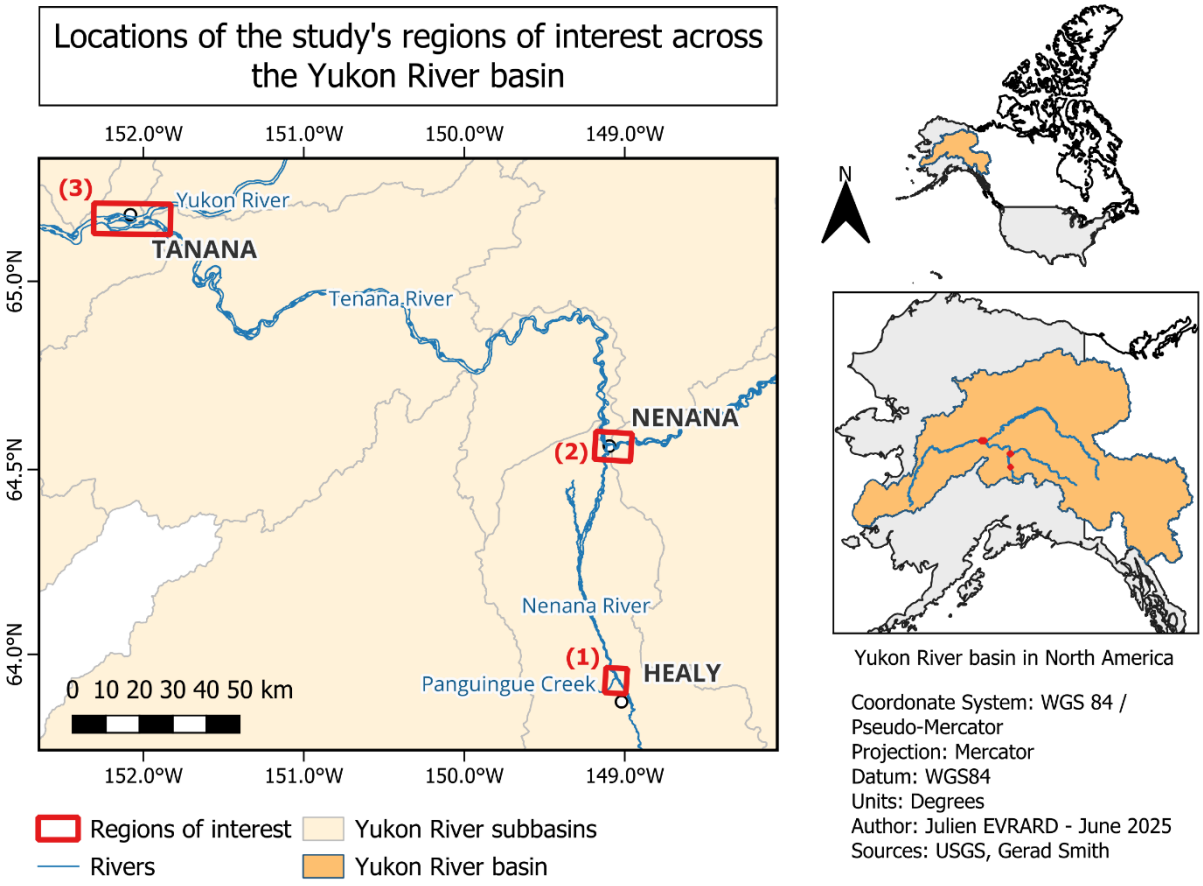


Figure 7: General locations of the three study's ROIs in the Yukon River basin: (1) Panguingue Creek ROI, (2) Nenana ROI and (3) Tanana rOI. Only the relevant rivers are shown for clarity purposes.

4.1. Panguingue Creek ROI

The first ROI covering the junction between Panguingue Creek and Nenana River, spans over 50 km² (Figure 8). The Nenana River then flows northbound. It partially covers the Panguingue Creek and Little Panguingue Creek-Nenana River subwatersheds, which respectively measures around 71 km² and 130 km² (USGS, 2025).

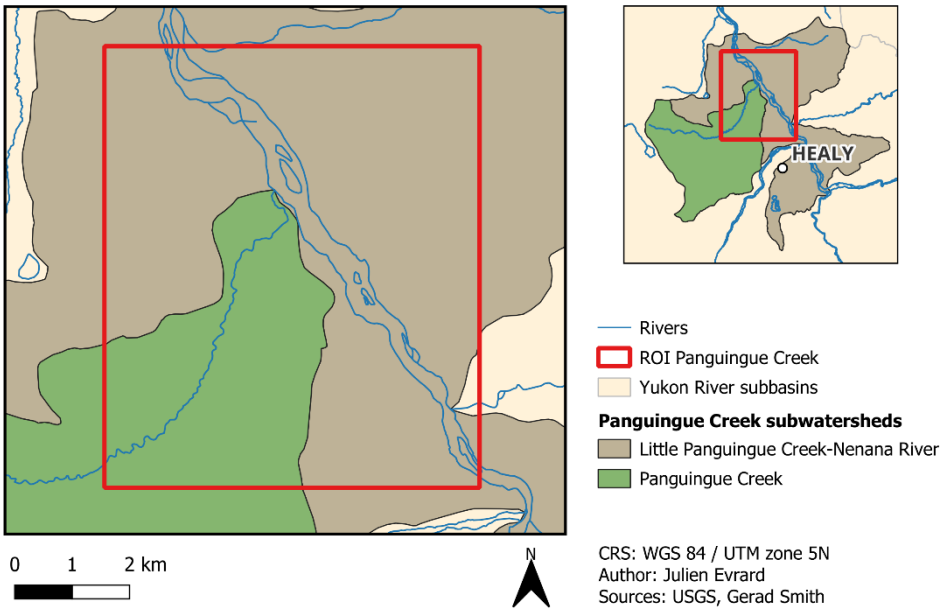


Figure 8: Delimitations, rivers and subwatersheds of the Panguingue Creek ROI.

4.2. Nenana ROI

The second ROI covers 90 km² (Figure 9). It is located at the the intersection of four river subwatersheds. The Nenana River flows into the Tanana River, which is headed west towards the Yukon River.

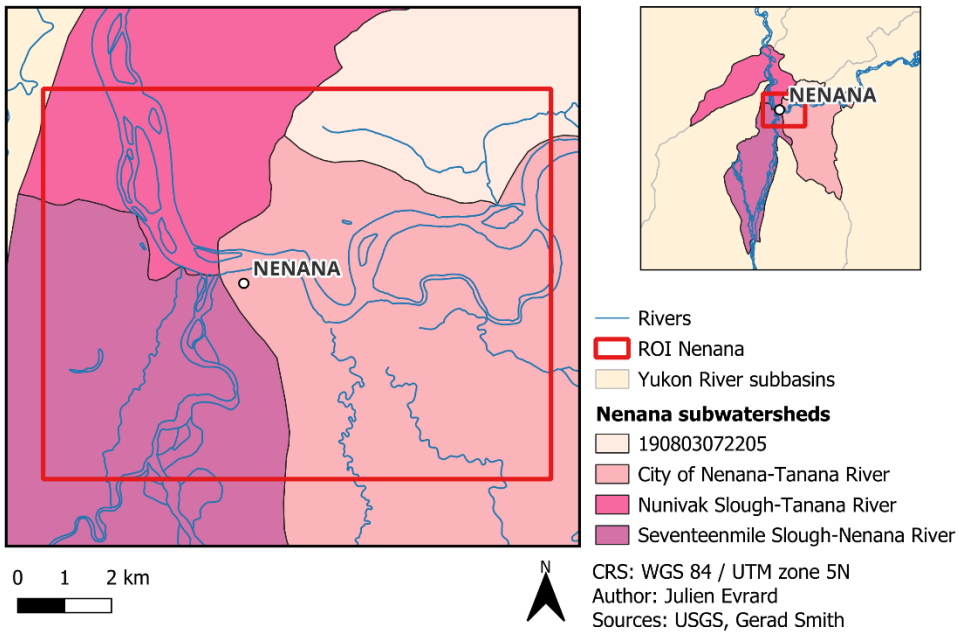


Figure 9: Delimitations, rivers and subwatersheds of the Nenana ROI.

4.3. Tanana ROI

The ROI encompassing the Tanana-Yukon River junction covers 200 km² (Figure 10). The Tanana River flows for over 150 km from Nenana, before merging into the Yukon River, which goes on westward. The ROI spans over ten subwatersheds.

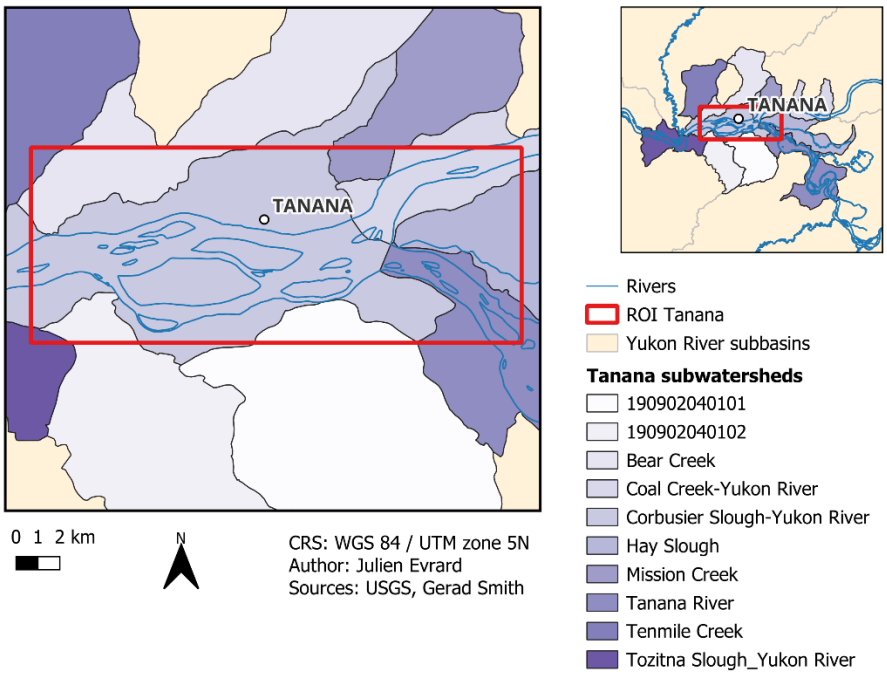


Figure 10: Delimitations, rivers and subwatersheds of the Tanana ROI.

4.4. Climate

The three ROIs are located in the Interior region of Alaska, which constitutes the largest area of the state. This region features a diverse terrain that includes both river valleys and highland areas. The climate is continental, characterized by high temperature fluctuations, low humidity, and relatively light and irregular precipitation. Summers are typically warm and sunny, whereas winters are very cold (Figure 11). Wind conditions are generally mild in the valleys, although wind speeds tend to increase during the summer months. A substantial portion of the annual precipitation occurs during the summer, primarily in the form of occasional rain showers or thunderstorms (Alaska Climate Research Center, n.d.-a).

For clarity purposes, a first order station in Fairbanks was used to illustrate the tree ROIs climate (Figure 11). That approximation was judged valid due to the station data being heavily quality checked and used to represent the region and the state (USGS, 2019). Small differences can exist due to altitude and geomorphological characteristics of each ROI.

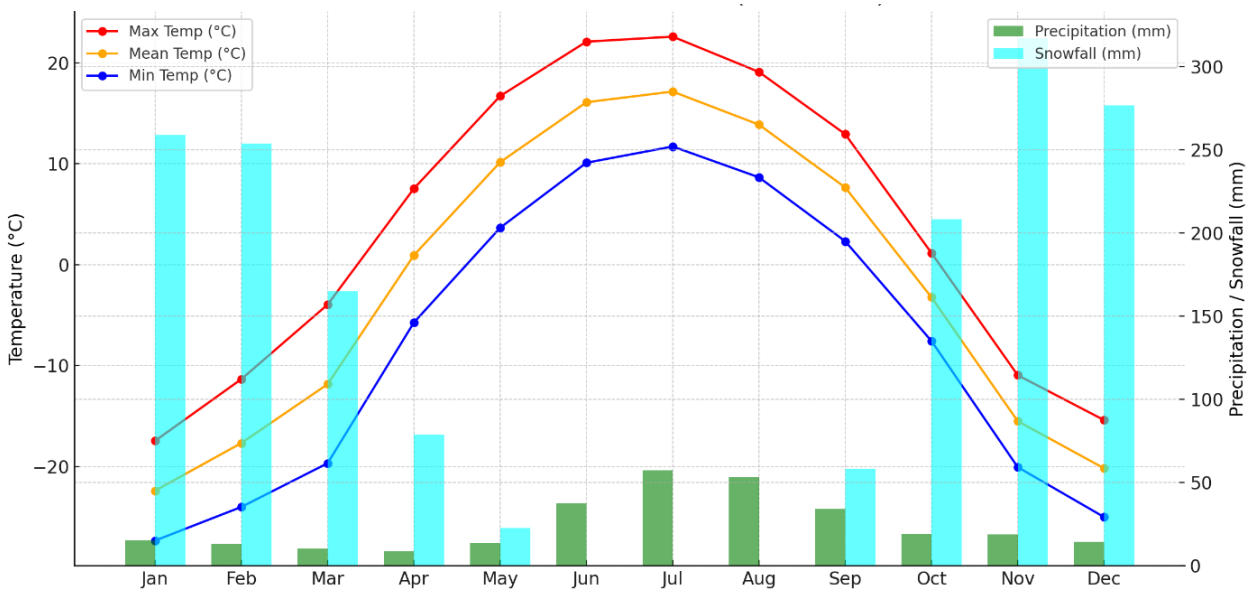


Figure 11: Temperatures, total precipitation and snowfall normals in Fairbanks for 1991-2020. In Fairbanks, since first observations in 1949 to 2020, seasonal temperature differences range from approximately 1.1°C in fall to 4.3°C in winter, with an annual average difference of about 2.3°C (Alaska Climate Research Center, n.d.-b).

In the Nenana ROI, comparison between breakup date normals over 90 years shows a clear period shift for the 1991-2020 period. It is close to a week earlier than 1931-1960 and 1961-1990 (Figure 12). Similar trends can be observed for other ROIs.

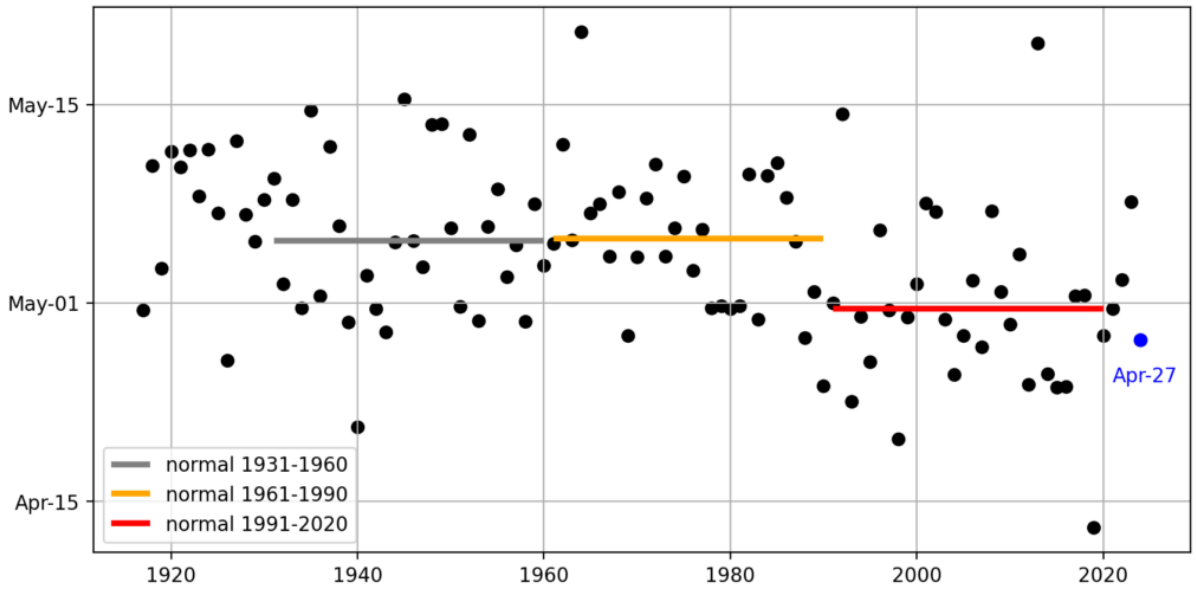


Figure 12: River break-up dates on the Tanana River at Nenana as recorded by the Nenana Ice Classic since 1917 until 2024. Average break-up dates for the climate reference periods 1931-1960, 1961-1990 and 1991-2020 are plotted as colored lines for reference. (Source: Alaska Climate Research Center; data from nsidc.org, nenanaakicceclassic.com)

5. Materials and methods

5.1. Data collection

5.1.1. *In situ* data

This study focused on the 2018 thawing season (April-May) to build on the *in situ* data collected by Opfergelt et al. at Panguingue Creek in 2018 (*Research – WeThaw*, n.d.).

Breakup dates

In 2018, the ice breakups happened in Panguingue Creek, Nenana River and Tanana River respectively the 10/05, 01/05 and 07/05.

Methods for recording break up dates vary. For Panguingue Creek it is based on the photographic imagery Sophie Opfergelt and her team took during one of their campaigns in 2018 (Figure 13).

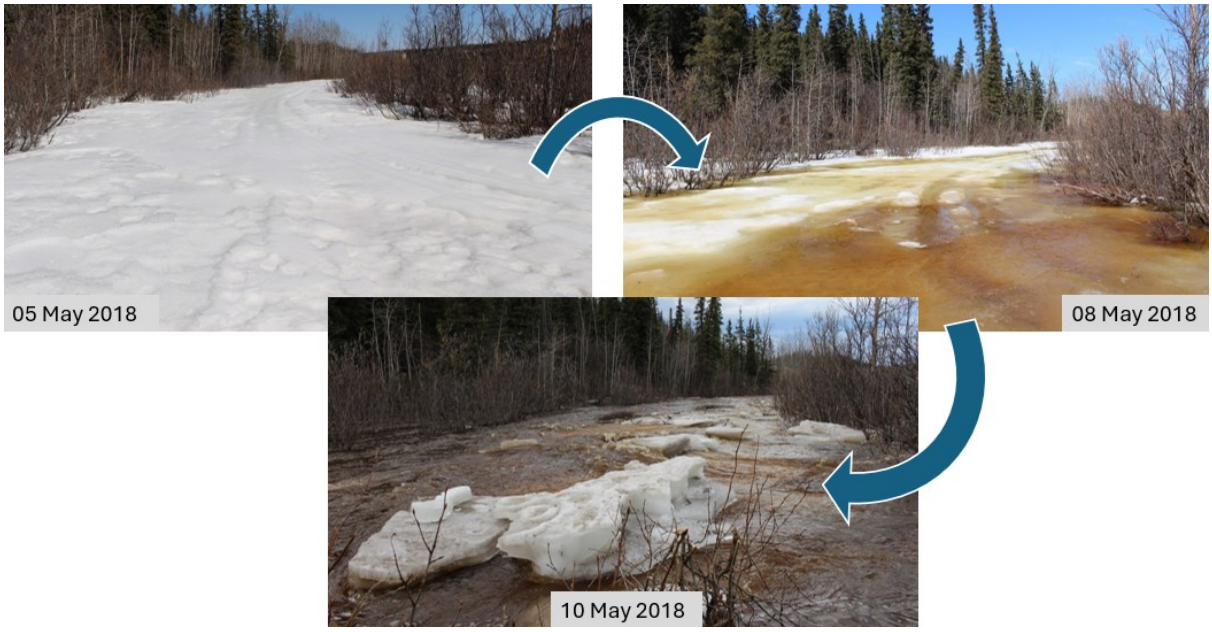


Figure 13: Evolution of river ice cover on Panguingue Creek in 2018 (Credit: Opfergelt et al.).

For the Nenana River, the data was retrieved from the National Oceanic and Atmospheric Administration (NOAA) breakup database **(NOAA, n.d.-a)**.

For the Tanana River, the data comes from the Nenana **Ice Classic,** an annual event started in 1906 where participants try to predict the exact date and time the ice will break on the Tanana River at Nenana city. Organizers place a tripod on the frozen river, and when the ice moves and the tripod tips, it triggers a clock that records the official time of breakup (Figure 14). The person whose guess is closest wins a monetary prize.



Figure 14: The Nenana Ice Classic tripod. Photo taken on March 24, 2009 (Credit: James Brooks).

Discharge

Daily discharge data from 01/04/2018 to the 10/06/2018 has only been found for the Tanana River. The station (USGS 15515500 TANANA R AT NENANA AK) provided estimated and recorded discharge from the Tanana River at Nenana.

The United States Geological Survey (USGS) estimates stream discharge primarily through the development and application of a stage-discharge relationship, known as a rating curve. A stream gage continuously records water stage (surface height) at the monitoring site. At regular intervals, USGS hydrologists conduct direct discharge measurements using instruments such as current meters or acoustic Doppler devices. These paired observations of stage and discharge are used to construct a rating curve, which allows for the estimation of discharge from continuous stage data.

Discharge values are marked as "estimated" when direct measurement is not possible or when the rating curve must be extrapolated beyond the range of measured data, such as during floods or droughts. Estimates are also used if ice, debris, or equipment issues affect stage readings, or if rapid channel changes alter the streambed and invalidate the existing rating curve. In these cases, the USGS relies on professional judgment, nearby data, or hydrologic modelling to provide the best possible estimate until new measurements can be obtained (USGS, 2019, 2024).

Air temperature

Daily air temperatures for the period from 01/04/2018 to the 10/06/2018 were retrieved from meteorological stations closest to the study areas as possible. For Panguingue Creek, data were collected and recorded using an Onset HOBO weather station 8 km away at Eight Mile Lake (Kennedy et al., 2025). NOAA's stations based in Calhoun Memorial Airport (Tanana) and Nenana Municipal Airport were used for the other study areas.

Ice thickness

Ice thickness measurements are relatively scarce. NOAA provide monthly ice thickness data and historical averages in the region, but only one data could be found in a range of 70 and 150 km around Panguingue Creek and Tanana River respectively, being in Nenana city. The Nenana Ice Classic (2018) recorded the last measurement at 25 inches or 63.5 cm thick on April 18, equal to 61% of the historical ice thickness average for the month of April (NOAA, n.d.-b).

Water temperature

The discontinuity in water temperature data limits its usefulness for identifying trends relevant to ice breakup detection. In Panguingue Creek, Opfergelt et al. measure daily water temperatures from the 03/05/18 to the 12/05/18. At Nenana River, available data starts after the breakup, on the 10/05 (USGS, n.d.). No measurements were found for Tanana River.

5.1.2. Satellite data

The Sentinel images were downloaded from the Copernicus Data Space Ecosystem Browser, an open access online platform with data from the Copernicus Sentinel constellations.

Sentinel-1

Sentinel-1 Ground Range Detected (GRD) products, available from the Copernicus Browser, are radar images processed from Level-1 Single Look Complex (SLC) data. The transition from SLC to GRD is performed to generate georeferenced, amplitude-only radar images that are easier to use for mapping and change detection. To create GRD products, the SLC data undergoes several processing steps: thermal noise removal, radiometric calibration to convert raw values to physically meaningful backscatter coefficients, and multilooking to reduce speckle and improve radiometric quality. The data is then detected (converting complex to amplitude), projected from slant range to ground range using an Earth ellipsoid model, and georeferenced. Optional steps such as speckle filtering, radiometric terrain correction, and orthorectification using a digital elevation model may be applied, but standard GRD products are typically only ellipsoid-corrected and not fully terrain-corrected or orthorectified unless explicitly labelled as such (ESA, n.d.).

Sentinel-1 GRD products were delivered at a spatial resolution of 20 m, resampled at 10 m and included two bands: VV (vertical transmit and vertical receive) and VH (vertical transmit and horizontal receive) (Table 1). Dual polarization improves land cover discrimination because VV and VH channels interact differently with surfaces: VV is more sensitive to roughness and structure, while VH responds more to volume scattering from vegetation or complex surfaces (Saal, 2023). Further processing was focussed on VV bands, as they were proven more accurate than VH bands for river ice cover changes, namely for ice to open water (Lund et al., 2022; Saal, 2023; Stonevicius et al., 2022).

Table 1: Sentinel-1 C-SAR bands polarisation and spatial resolution

C-band number	Polarisation	Spatial resolution [m]
B01	VV	20
B02	VH	20
B03	VV/VH Ratio	20

The Sentinel-1 mission consists of twin satellites, Sentinel-1A and Sentinel-1B, whose orbits alternate between ascending and descending passes, enabling observation of the Earth's surface from opposite directions. As a result, ascending and descending passes view the surface from different angles, introducing geometric differences that influence the backscatter signal (Figure 15). This complicates direct comparison when monitoring rapid changes like ice breakup, as observed differences may result from viewing geometry variation rather than actual surface change.

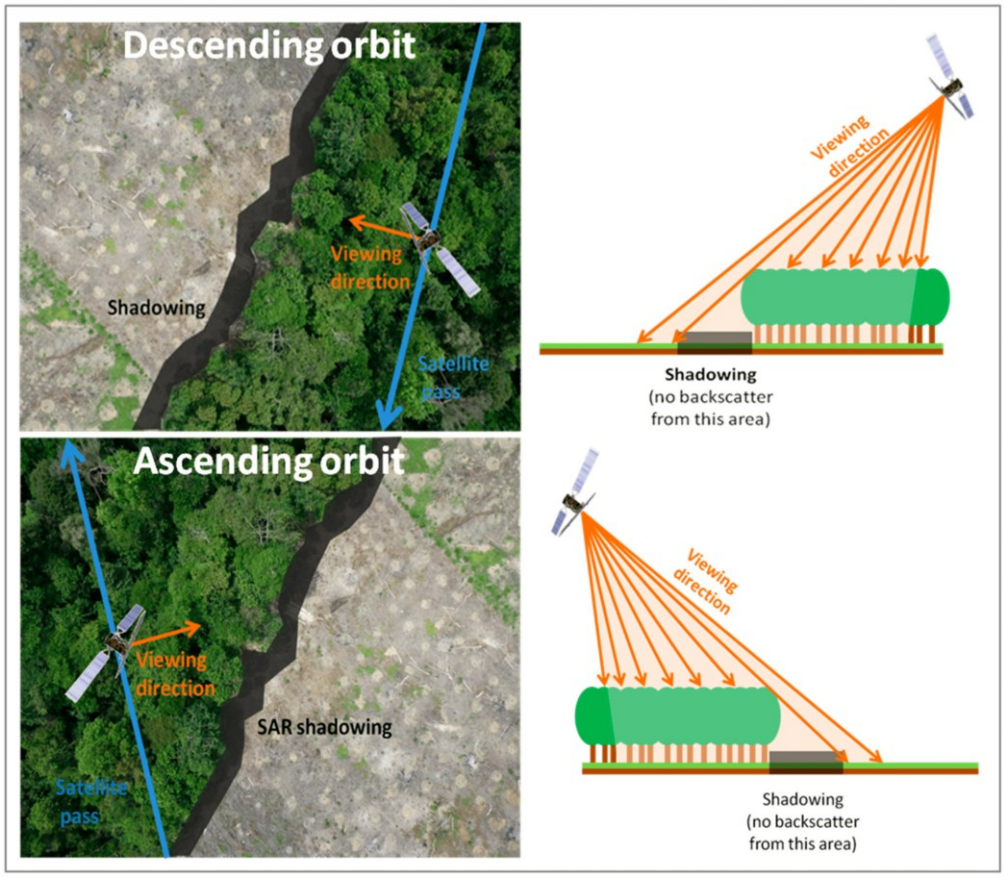


Figure 15: Changes in backscatter signal due to the difference between ascending and descending orbit (Bouvet et al., 2018)

To minimize the influence of geometric differences between ascending and descending passes, only a single pass direction was selected for analysis, based on data availability. The ascending pass was chosen as it provided the greatest number of usable images.

Although the theoretical Sentinel-1 revisit time is 12 days, overlapping swaths in the Panguingue Creek and Nenana ROIs reduced the effective temporal resolution to between two and ten days. For the Tanana ROI, the same approach was applied, but using the descending pass.

This resulted in the following set of useful acquisition dates for Sentinel-1 by ROI:

- Panguingue Creek: 12, 22, 24 April 2018; 4, 6, 18, 28 May 2018
- Nenana: 12, 22, 24 April 2018; 4, 6, 18, 28 May 2018
- Tanana: 22 April 2018; 4, 28 May 2018

Sentinel-2

Sentinel-2 data were downloaded as already pre-processed ESA products. The Level-2A (L2A) product delivers atmospherically corrected Bottom-Of-Atmosphere (BOA) surface-reflectance images, derived from Level-1C (L1C) Top-Of-Atmosphere (TOA) products. L2A includes a Scene Classification Layer (SCL) that labels clouds, cloud shadows, vegetation, soils/deserts, water, and snow. Sen2Cor's modules transform L1C into L2A outputs by correcting the absorption and scattering of air molecules, of atmospheric gases (ozone, oxygen, water vapour) and aerosol particles. All spectral bands and the SCL are orthorectified with sub-pixel multispectral registration and resampled to 10 m, 20 m, or 60 m resolutions (Table 2).

Table 2: Spectral resolution of the Sentinel-2 bands used for this study

Band number	Band name	Central wavelength [nm]	Spatial Resolution [m]
B01	Coastal aerosol	443	60
B02	Blue	490	10
B03	Green	560	10
B04	Red	665	10
B05	Vegetation Red Edge	705	20
B06	Vegetation Red Edge	740	20
B07	Vegetation Red Edge	783	20
B08	Near InfraRed (NIR)	842	10
B8A	Narrow NIR	865	20
B09	Water vapour	945	60
B11	Short-Wave InfraRed (SWIR)	1610	20
B12	SWIR	2190	20

Scenes with excessive cloud cover were excluded to ensure reliable visual and pixel-based analyses. The study targeted the mid-April to late-May period to capture successive ice breakup stages. The remaining, mostly cloud-free acquisition dates per ROI for Sentinel-2 are:

- Panguingue Creek: 16, 18, 21, 25 April 2018; 5, 8, 15, 21, 28 May 2018
- Nenana: 16, 18, 21, 25 April 2018; 5, 8, 10, 13, 28 May 2018
- Tanana: 14, 16, 19, 21 April 2018: 29 May 2018

These images, still containing clouds, were therefore processed with the SCL mask to identify and retain only dates with sufficient usable pixels for future classification. Images that didn't pass this threshold could be kept for visual analysis.

PlanetScope

PlanetScope images were recovered for the three ROIs, using Dove Classic imagery. Dove Classic imagery is captured by the PS2 instrument, which acquire four spectral bands: red, green, blue, and NIR (Table 3). The products delivered have harmonized Surface Reflectance (SR) values, orthorectified to a cartographic projection. Key preprocessing steps include radiometric calibration using on-orbit calibration, geometric correction with Digital Elevation Models (DEMs) and ground control points for heightened positional accuracy, and harmonization to Sentinel-2 reflectance standards for cross-sensor consistency.

Table 3: Spectral resolution of the PlanetScope data used for this study

Band number	Name	Central Wavelength [nm]	Spatial resolution [m]
B01	Blue	485	3.7
B02	Green	545	3.7
B03	Red	630	3.7
B04	NIR	820	3.7

PlanetScope images were used for visual validation. Therefore, images on the day of sentinel-1 and Sentinel-2 images. As optical imagery, Cloud cover influence data. Availability by ROI:

The remaining, mostly cloud-free acquisition dates per ROI for PlanetScope are:

- **Panguingue Creek:** 12, 16, 18, 21, 22, 25 April 2018; 5, 8, 15, 28 May 2018
- **Nenana:** 12, 16, 18, 21, 22 April 2018; 5, 8, 10, 13, 22, 28 May 2018
- **Tanana:** 14, 16, 19, 21, 22 April 2018: 29 May 2018

5.2. Spectral indices

Spectral indices and composites were applied to satellite data (Sentinel-2 and PlanetScope) to enhance feature discrimination during polygon digitization and validation (Table 4). Normalized Difference Snow Index (NDSI) and Normalized Difference Water Index (NDWI) were omitted due to poor discrimination between snow and open water and salt-and-pepper noise during thaw conditions.

Table 4: Summary of each spectral index or composite, its primary highlight, and the bands or formula used.

Index / Composite	Highlight	Bands / Formula
True Colour Composite	Natural-looking image with balanced clouds and snow brightness	Sentinel-2: B04, B03, B02 PlanetScope: B03, B02, B01
Highlight-Optimized Natural Colour	Even exposure and no burn-out in bright areas	Sentinel-2: $\sqrt[3]{0.6 \times BO4}$, $\sqrt[3]{0.6 \times BO3}$, $\sqrt[3]{0.6 \times BO2}$
False Colour Composite	Vegetation health and density in red, snow and ice appear pale or white, water appears dark blue or black	Sentinel-2: B08, B04, B02
False Urban Composite	Urban areas in white/grey/purple; vegetation in green; snow and ice dark in blue; water in black	Sentinel-2: B12, B11, B04
SWIR False Colour Composite	Water bodies and wet soil in black; snow and ice in bright white; vegetation in green; soils and urban areas in brown	Sentinel-2: B12, B8A, B04
Normalized Difference Vegetation Index (NDVI)	Quantifies live green vegetation. The value range is -1 to 1. Barren areas of rock, sand, or snow near 0; water near –1; vegetation above 0.2	Sentinel-2: $(B08 - B04) / (B08 + B04)$

5.3. Sentinel-2 mapping of river ice cover

All pre-processing and processing of remote sensing imagery was done in QGIS 3.40.6, an open-access GIS software, either with the embedded Python Console or with plugins.

5.3.1. Pre-processing

To ensure consistent pixel dimensions across all spectral bands, resampling of Sentinel-2 imagery was required prior to analysis (Figure 16).

Different resampling methods were applied depending on the data type. Categorical data were resampled using the Nearest Neighbour method, which assigns output cell values based on the nearest input cell centre. This approach preserves the original pixel values. Continuous data were resampled using Bilinear Interpolation, which computes output values as a weighted average of the four nearest input cells. This method reduces the salt-and-pepper effect and ensures smoother transitions. Specifically, the 20 m and 60 m spectral bands were resampled using Bilinear Interpolation, while the SCL, a categorical dataset, was resampled to 10 m resolution using the Nearest Neighbour method.

To reduce computational load, all bands were clipped to the extent of the ROIs. A cloud screening process was subsequently applied using the resampled SCL, masking clouds, cloud shadows, and other unwanted classes, while retaining snow cover. Masked pixels were assigned a No Data value of −10,000 and excluded from further analysis. To capture the dynamics of ice breakup, four Sentinel-2 acquisition dates were selected between the remaining usable images to represent the stages before, nearest to, and after ice breakup: 16/04, 25/04, 05/05, and 28/05/18.

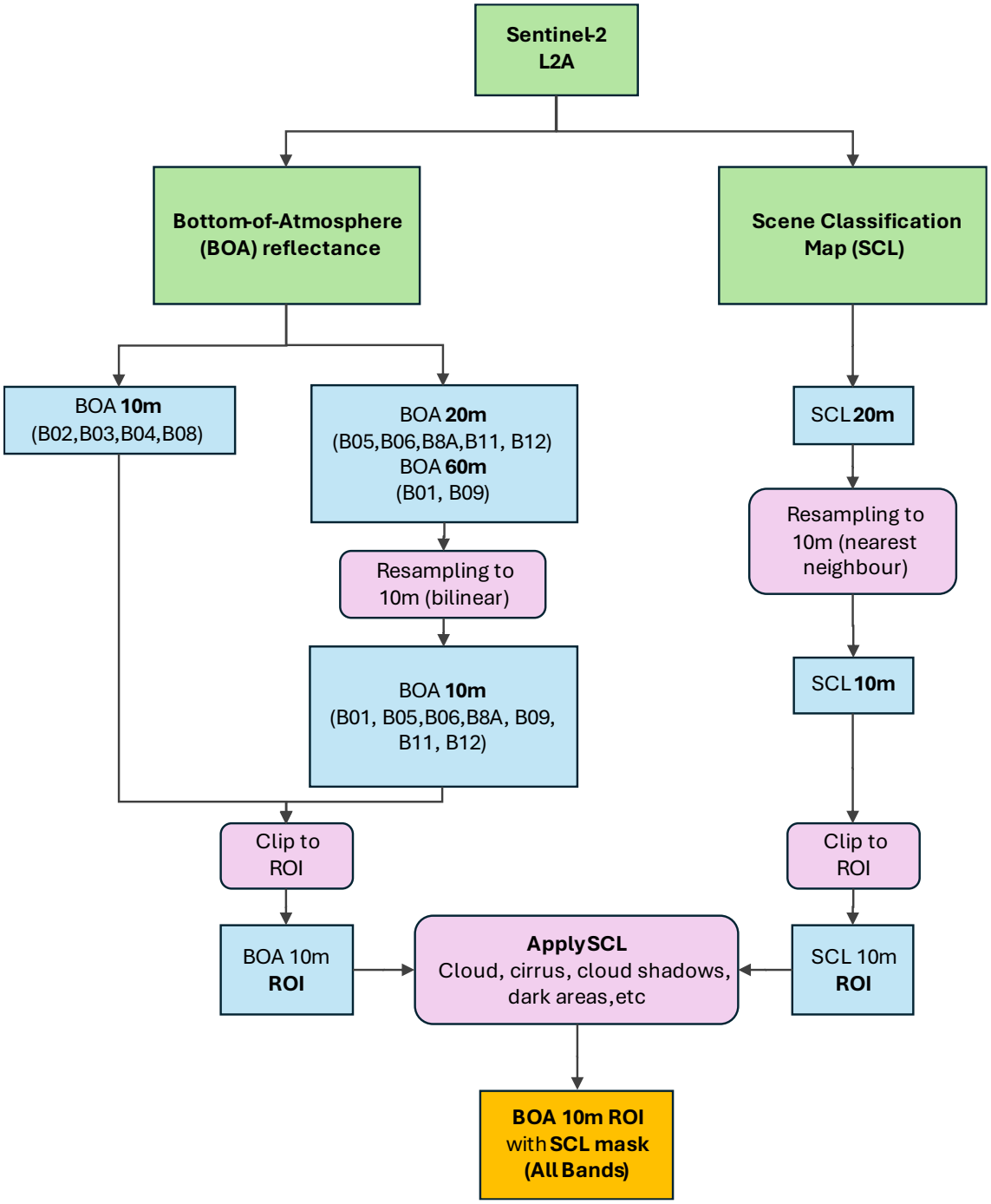


Figure 16: Sentinel-2 L2A pre-processing workflow, done in QGIS Python Console Plugin

5.3.2. Processing

Model dataset creation

Sample polygons were created through photo-interpretation using spectral indices, with each polygon assigned a land cover class. These polygons encompassed all relevant pixels for their respective classes. To capture intra-class variability and improve classification accuracy, care was taken to include diverse spectral responses within each class. The polygon dataset was adjusted according to each image dates, as land cover can shift daily under rapidly changing conditions such as ice breakup and thawing.

Seven land cover classes were defined: water, urban, bare soil, vegetation, snow, melting snow, and ice. An additional class was included for No Data pixels, resulting from the SCL mask.

Model Training and Classification

Sample polygons were put into a Random Forest (RF) classification algorithm using the Dzetsaka plugin (Karasiak, 2016). The classification required a raster image (All bands BOA 10m clipped to ROI with SCL mask) and a shapefile of sample polygons containing numeric class identifiers (1, 2, 3, etc), as text-based class identifiers were not supported by the plugin.

Model Validation

Due to limitations in Dzetsaka's built-in validation tools, the Accuracy Assessment of Thematic Maps (AcATaMa) plugin was used for accuracy evaluation (*AcATaMa*, n.d.). AcATaMa incorporates a sampling design for selecting reference data, a response design for defining evaluation protocols, and statistical analysis procedures using multiple estimators.

Stratified random sampling was employed to ensure rare classes were adequately represented and to reduce standard errors. Indeed, this method divides the population of samples into distinct groups and randomly selects samples from each, proportionally to their area, to ensure a fair representation of the different groups.

This method is recommended by Olofsson et al. (2014) for improving accuracy and spatial distribution in reference samples. A minimum of 50 samples per stratum was used, consistent with recommendations by Stehman & Foody (2019). The expected standard error of overall accuracy was set to 3% to balance accuracy and manageable sample sizes.



Figure 17: Stratified random sampling design (AcATaMa, n.d)

For example, RF classification on 25 April required for:

- 5% error: ~350 samples
- 3% error: ~374 samples
- 1% error: ~1666 samples

Each sample is then visualised through the response design module, using multiple synchronized data layers in a grid layout (Figure 17). Then, samples are assigned to class labels based on the available reference data.

Finally, a confusion matrix was generated to evaluate classification accuracy, comparing predicted *versus* actual classes. It enabled the calculation of key metrics such as overall accuracy, user's and producer's accuracies. Overall accuracy (OA) represents the proportion of correctly classified samples out of the total sample set and offers a general measure of classification performance. However, it does not account for errors at the class level. Producer's accuracy (PA) quantifies the proportion of reference (ground truth) samples correctly classified within a specific class, capturing omission errors and reflecting how well the classification process represents actual conditions. In contrast, user's accuracy (UA) measures the proportion of classified samples that are correct for a particular class, indicating the probability that a map label accurately corresponds to ground conditions and addressing commission errors from the map user's perspective.

5.4. Sentinel-1 backscatter change detection

All data preprocessing and analysis were conducted entirely within QGIS 3.40.6. This workflow focuses on detecting both absolute and relative changes in backscatter intensity between image pairs using QGIS's native raster tools.

5.4.1. Pre-processing

To ensure consistent pixel dimensions across all bands between images, resampling of Sentinel-1 imagery was required prior to analysis. In the downloaded GRD Sentinel-1 data, minor deviations from the 10 m spacing were corrected using nearest neighbour interpolation to standardize the spatial grid prior to analysis. Furthermore, to reduce computational load, all bands were clipped to the extent of the ROIs. Clipping was performed with shapefiles representing ROIs, used as masks. This step considerably reduced the spatial extent of each raster, limiting subsequent processing to more manageable areas (50 to 90 km² depending on the ROI) rather than the full GRD tile of nearly 2,000 km². The resulting clipped rasters serve as the inputs for change detection. Given the exclusive use of data from the same orbit direction for each site, the GRD radar preprocessing chain was deemed sufficient for the purposes of simple change detection. Caution must be applied when using this estimation, as speckle noise and the lack of terrain correction can alter backscatter values.

5.4.2. Processing

To compute changes in backscatter between two dates, the QGIS *Raster Calculator* was used to perform pixel-wise subtraction between corresponding clipped rasters. Two types of changes were computed: absolute and relative change. For absolute change, the following expression was entered in *Raster Calculator*:

$$Image_{t2} - Image_{t1} \quad [1]$$

where $Image_{t2}$ is the image on the date following $Image_{t1}$. It gives a raster in linear format.

To compute relative change, data is transformed into decibels (dB) and then subtracted following formula:

$$10 * \log 10\,(Image_{t2}) - 10 * \log 10\,(Image_{t1}) \quad [2]$$

When comparing radar backscatter data in linear and decibels (dB) formats, several practical differences arise that affect change detection workflows. In linear format, visual contrast between water and ice or snow is typically high, as water pixels tend to cluster near zero while ice and snow return higher values. In contrast, dB data compress this dynamic range and zero centres it, which can reduce visual contrast but improves interpretability.

Due to geometry mismatch between the two swaths for the Panguingue Creek ROI, the data was split into two time series to ensure that identified change wasn't artificially created by misaligned pixels between two dates. The newly created time series are:

- 12, 24, April 2018; 06, 18 May 2018
- 22 April 2018; 04, 28 May 2018.

For the Nenana ROI, only the 28 May was misaligned with the other images, and was removed from the sample. It was deemed not so consequential as breakup happens on the 1st of May, and imagery on the 04, 06, 18 May exists beforehand, giving sufficient post breakup data.

Outputs where finally validated with optical imagery (PlanetScope and Sentinel-2), to determine whether or not ice breakup was correctly identified, and until which river size it was possible to derive change.

6. Results

The results are structured around two main axes: temporal resolution and spatial resolution. This approach makes it possible to assess the extent to which the available data help reduce uncertainty regarding the timing of river ice breakup, by combining observation frequency and detection capability according to river size.

6.1. Temporal resolution

6.1.1. Satellite imagery

The temporal analysis is based on identifying the periods during which satellite imagery (Sentinel-1, Sentinel-2, PlanetScope) can be effectively used to detect the timing of river ice breakup. A preliminary sorting of the images was conducted using a cloud-filtering method applied to Sentinel-2 data, based on the percentage of cloud cover indicated in the scene metadata. Only images for which atmospheric conditions allowed for reliable interpretation were retained. As an example, the methodology is illustrated for the Panguingue Creek ROI in Figure 18. The same approach was applied to the Nenana and Tanana ROIs (not shown here).

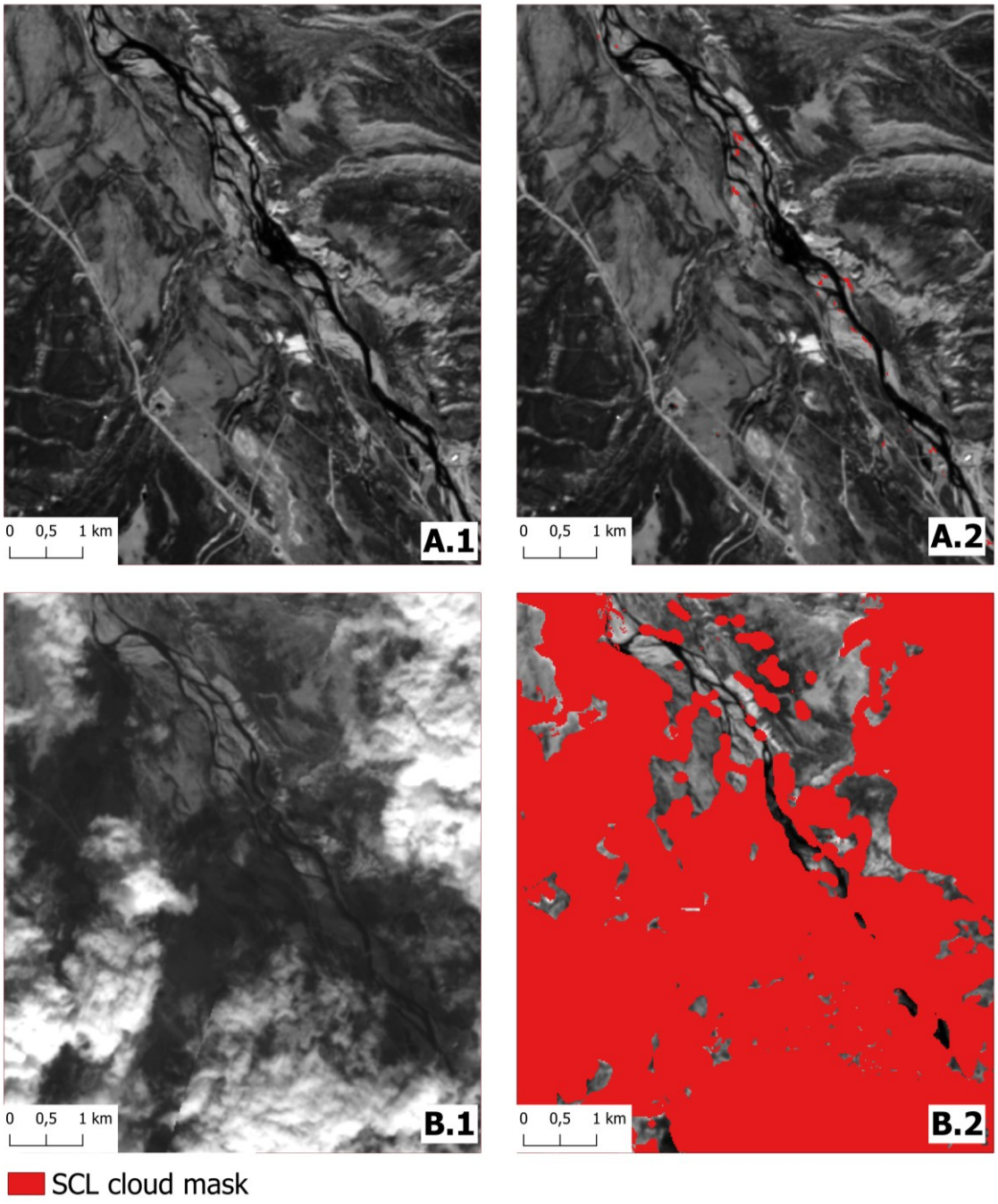


Figure 18: Before and after SCL cloud mask was applied on Sentinel-2 imagery for the ROI of Panguingue Creek. A.1) and A.2) show the result on the B12 band for the 05/05, while B.1) and B.2) show the result on the B12 band for the 13/05. Based on the coverage of the SCL cloud mask, 13/05 was removed from the data pool.

This step made it possible to produce a graph showing the actual availability of imagery around the breakup period for each study site (Figure 19Figure 18). Valid satellite imagery is available for each ROI, but to different extents.

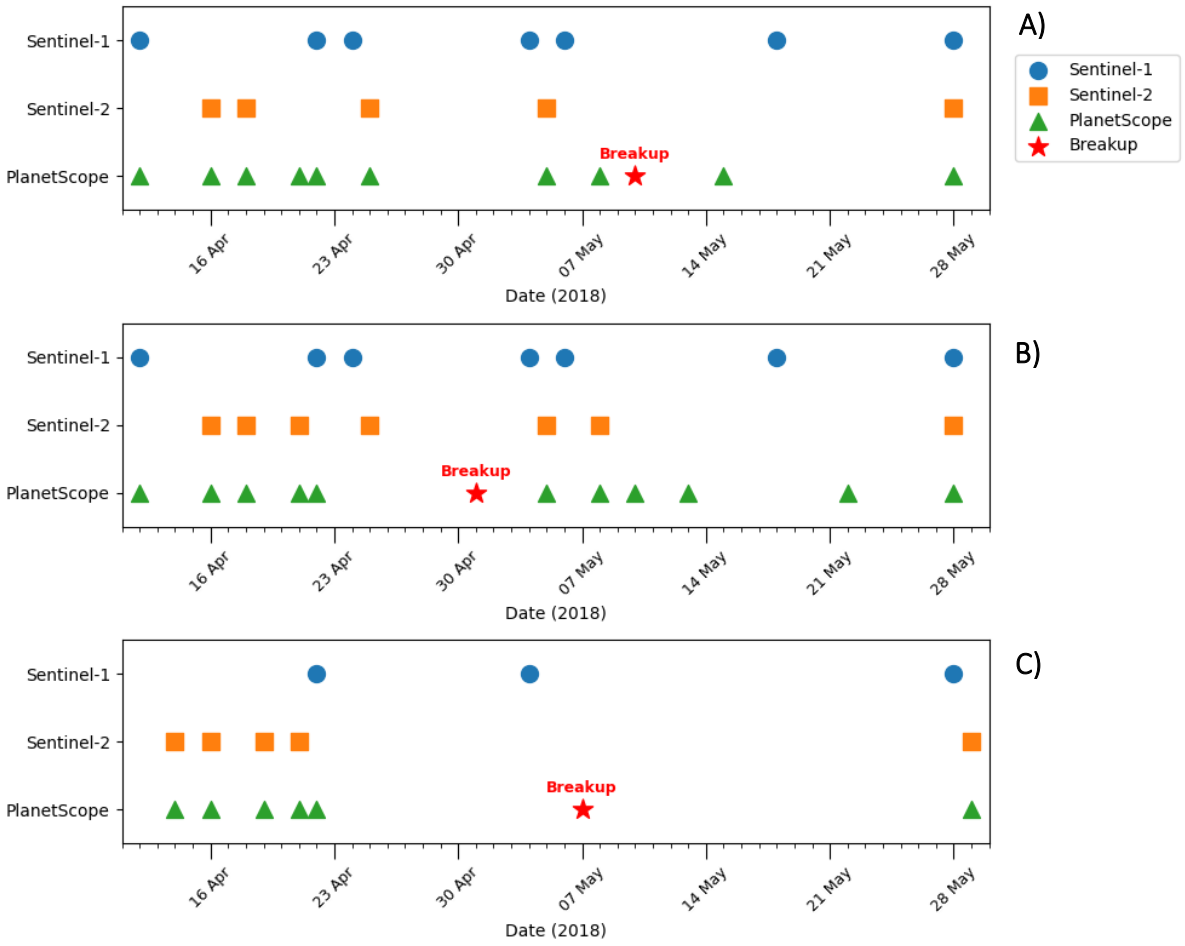


Figure 19: Sentinel-1, Sentinel-2 and PlanetScope data availability during the 2018 thawing season (April to May) for the different ROIs. For Sentinel-2, the data available passed the SCL test. Breakup dates for each ROI is highlighted in red. A) Panguingue Creek ROI; B) Nenana ROI; C) Tanana ROI.

Breakup dates from *in situ* data (Photographic evidence Panguingue Creek, official measurement from Nenana Ice Classic, NOAA for Tenana) are confronted with the dates of valid satellite acquisitions. This comparison allows for the definition of a detection window, which corresponds to the time interval between the last image showing no sign of break-up and the first image indicating a change, such as ice fracture or the presence of open water. For Panguingue Creek, the detection window is estimated at 12 days for Sentinel-1 and 23 days for both Sentinel-2 and PlanetScope. For Nenana, the detection window is estimated at 12 days for Sentinel-1 and 10 days for both Sentinel-2 and PlanetScope. For Tanana, the detection window is estimated at 24 days for Sentinel-1 and 39 days for both Sentinel-2 and PlanetScope. These results help to identify the minimum time lag between the actual occurrence of the event and its detection in satellite imagery. This lag is referred to as the observation delay. One precision is that in this study, Planetscope images are mainly used for validating Sentinel-1 and Sentinel-2 images. There may be available Planetscope images on days without Sentinel-1 or Sentinel-2 images, but they weren't considered in this work.

6.1.2. In situ data

In situ data of environmental variables such as air temperature, river discharge (when available), and ice thickness (when available) were analysed as time series (Figure 20).



Figure 20: Daily mean air temperature (°C) and breakup dates for each ROI, and daily mean discharge (m³/s) for Nenana ROI. A) Panguingue Creek ROI; B) Nenana ROI ; C) Tanana ROI. Mean discharge is directly measured from station data. Estimated mean discharge is based on

expert judgement (USGS, 2019, 2024). Data ranging from April 1 2018 to June 10 2018. (Source: Alaska Climate Research Center (https://akclimate.org))

At the Panguingue Creek, Nenana, and Tanana ROIs, daily mean air temperatures consecutively exceed 0 °C several days prior to the observed breakup. This occurs respectively 6, 8, and 12 days before the event.

At Nenana (where the discharge data are available), a marked increase in river discharge is observed starting three days after the breakup. A first peak in discharge, reaching approximately 1,470 m^3/s, occurs on May 13, twelve days after the breakup. It is important to note that mean discharge values are estimated prior to May 15. Discharge data for Arctic rivers during the winter months reflect periods when direct measurements are not possible due to ice cover. The USGS relies on models, historical data, and expert judgment from its hydrologists to produce the best possible estimates.

Ice thickness data are available sparsely only for the Nenana ROI. The last measurement prior to breakup, taken on April 18, indicated an ice thickness of 0.63 m. While this value provides a useful reference point, it remains too limited to support a systematic analysis.

Water temperature was excluded from this study, as the observation sites are not instrumented during frozen periods, and no validated expert-based modelling is currently available at the regional scale.

6.2. Spatial resolution

Given the limited availability of field data and satellite imagery for the Tanana ROI (Figure 19), this analysis of the spatial resolution, will be focused on the Nenana ROI and the Panguingue Creek ROI, as these ROIs provided a more comprehensive dataset for investigation.

6.2.1. Spectral analysis – Sentinel-2 Random Forest Classification

To assess the ability of satellites to detect river ice breakup relative to stream width, supervised Random Forest classifications were applied to spectral bands of Sentinel-2 images, acquired at different dates around the breakup. Results are presented first for the Panguingue Creek ROI, then for the Nenana ROI.

Random Forest Classification - Panguingue Creek

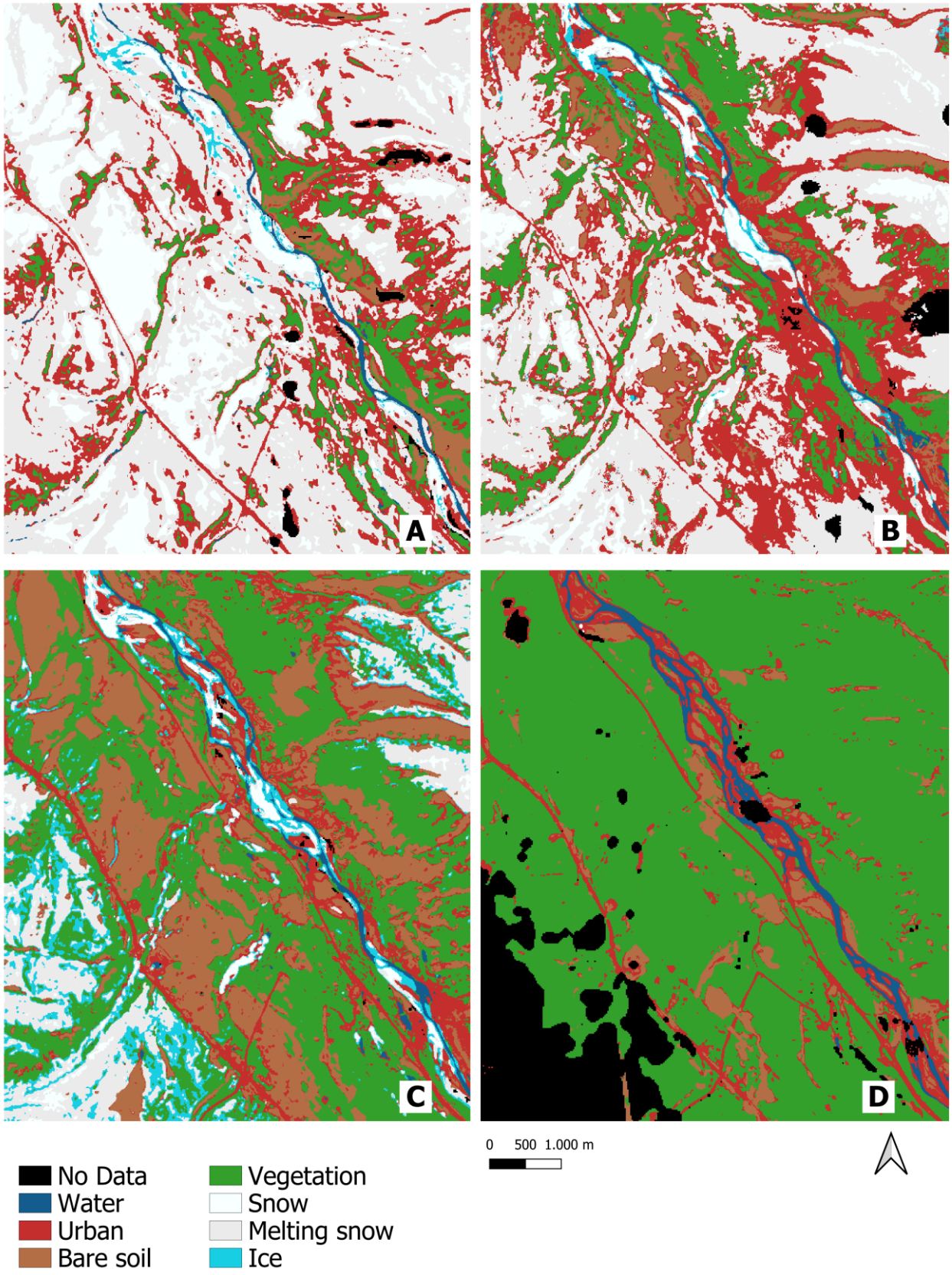


Figure 21: Temporal series of Panguingue Creek ROI's land cover, based on Random Forest classifications of Sentinel-2 data. A) 16/04; B) 25/04; C) 05/05; D) 28/05.

Table 5: Key results of Panguingue Creek Random Forest classifications (16/04; 25/04; 05/05; 28/05): overall, producer, and user accuracies of the classes of interest (Water, Snow, Melting snow, and Ice), where n= number of samples.

	16-Apr (n=390)		25-Apr (n=374)		05-May (n=366)		28-May (n=344)	
Class	Prod. Acc. [%]	User acc. [%]	Prod. Acc. [%]	User acc. [%]	Prod. Acc. [%]	User acc. [%]	Prod. Acc. [%]	User acc. [%]
Water	69	74	93	68	80	86	66	100
Snow	92	90	87	88	88	100	100	94
Melting snow	79	98	72	99	58	98	/	/
Ice	100	58	90	58	98	14	/	/
	Overall Acc. [%]		Overall Acc. [%]		Overall Acc. [%]		Overall Acc. [%]	
	79±1		71±2		74±2		88±1	

The Random Forest classifications results for Panguingue Creek demonstrate variable classification performance across four Sentinel-2 acquisition dates: 16 April, 25 April, 5 May, and 28 May 2018 (Table 5). The key results of each class (overall, producer, and user accuracies) are showcased. The number of reference samples used per date ranges from 344 to 390. Results pertaining the NoData, Urban, Bare soil and Vegetation classes aren't showcased here to focus on the classes relevant to ice and river detection.

On 16 April, the classification achieved an overall accuracy of 79% (±1%). Producer's accuracies reached 100% for Ice, 92% for Snow, 79% for Melting Snow, and 69% for Water. Corresponding user's accuracies were 58% for Ice, 90% for Snow, 98% for Melting Snow, and 74% for Water.

On 25 April, the classification produced an overall accuracy of 71% (±2%). Producer's accuracies were 90% for Ice, 87% for Snow, 72% for Melting Snow, and 93% for Water. User's accuracies were 58% for Ice, 88% for Snow, 99% for Melting Snow, and 68% for Water.

On 5 May, the classification achieved an overall accuracy of 74% (±2%). Producer's accuracies reached 98% for Ice, 88% for Snow, 58% for Melting Snow, and 80% for Water. User's accuracies were 14% for Ice, 100% for Snow, 98% for Melting Snow, and 86% for Water.

On 28 May, the classification yielded an overall accuracy of 88% (±1%). Only Water and Snow classes were detected. Producer's accuracies were 66% for Water and 100% for Snow. User's accuracies were 100% for Water and 94% for Snow.

Random Forest Classification - Nenana

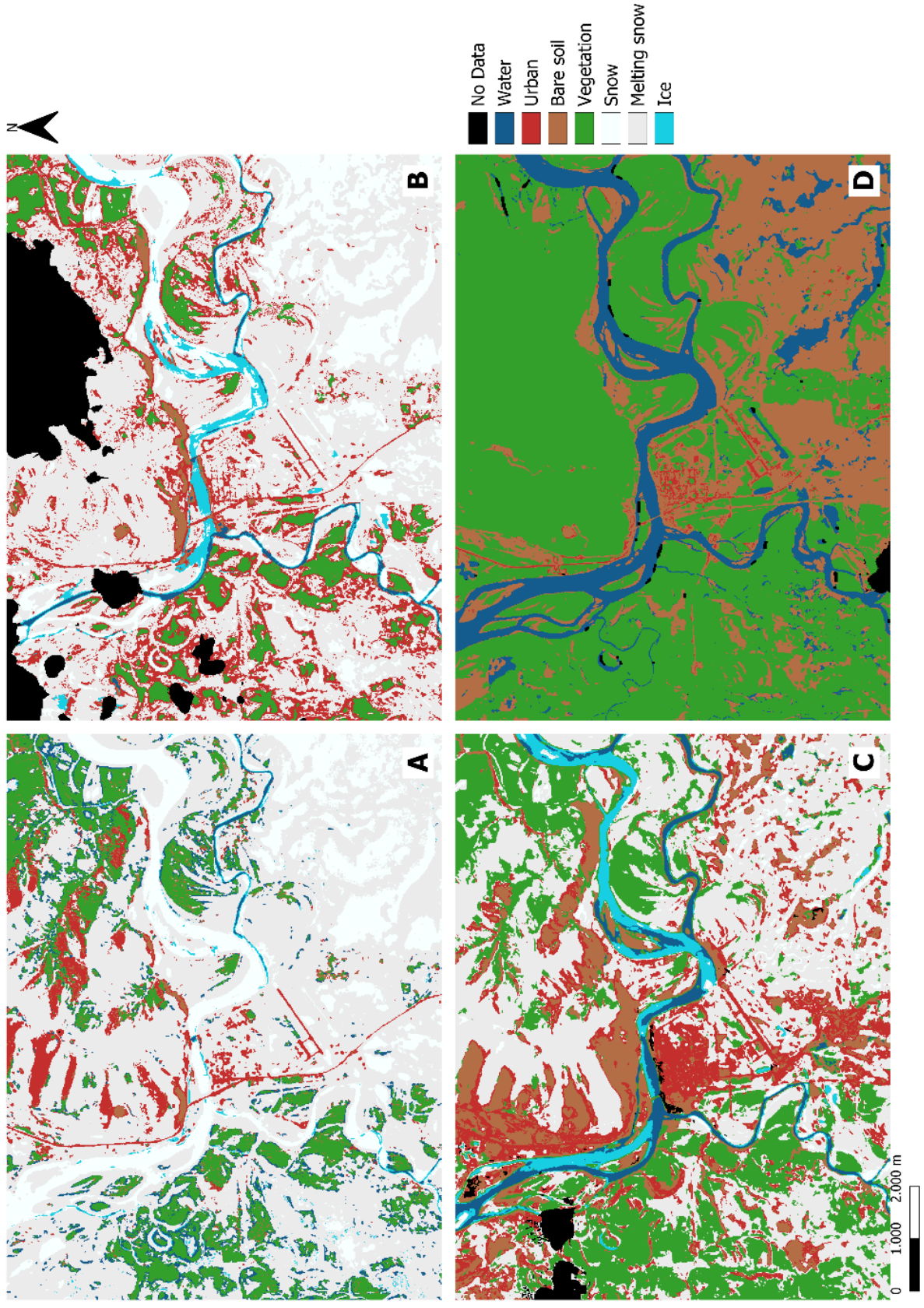


Figure 22: Temporal series of Nenana ROI's land cover, based on Random Forest classifications of Sentinel-2 data. A) 16/04; B) 25/04; C) 05/05; D) 28/05.

Table 6: Key results of Nenana Random Forest classifications (16/04; 25/04; 05/05; 28/05). Here are represented the overall, producer, and user accuracies of the classes of interest (Water, Snow, Melting snow, and Ice), where n= number of samples.

	16-Apr (n=405)		25-Apr (n=402)		05-May (n=378)		28-May (n=256)	
Class	Prod. Acc. [%]	User acc. [%]	Prod. Acc. [%]	User acc. [%]	Prod. Acc. [%]	User acc. [%]	Prod. Acc. [%]	User acc. [%]
Water	91	6	88	96	76	96	100	82
Snow	75	98	79	100	42	100	/	/
Melting snow	83	90	83	93	87	86	/	/
Ice	72	36	87	82	100	78	/	/
	Overall Acc. [%]		Overall Acc. [%]		Overall Acc. [%]		Overall Acc. [%]	
	79±2		81±2		77±2		89±2	

The Random Forest classifications in the Nenana ROI produced varying results across four Sentinel-2 acquisition dates (Table 7): 16 April, 25 April, 5 May, and 28 May 2018. The analysis focuses on the Water, Snow, Melting Snow, and Ice classes, which are relevant to river and ice monitoring. It excludes the NoData, Urban, Bare Soil, and Vegetation classes. The number of reference samples per date ranges from 256 to 405. For each date, the overall accuracy (± standard deviation) is reported along with class-specific producer's and user's accuracies.

On 16 April, the classification achieved an overall accuracy of 79% (±2%). Producer's accuracies reached 91% for Water, 75% for Snow, 83% for Melting Snow, and 72% for Ice. Corresponding user's accuracies were 6% for Water, 98% for Snow, 90% for Melting Snow, and 36% for Ice.

On 25 April, the overall accuracy was 81% (±2%). Producer's accuracies were 88% for Water, 79% for Snow, 83% for Melting Snow, and 87% for Ice. User's accuracies reached 96% for Water, 100% for Snow, 93% for Melting Snow, and 82% for Ice.

On 5 May, the classification produced an overall accuracy of 77% (±2%). Producer's accuracies were 76% for Water, 42% for Snow, 87% for Melting Snow, and 100% for Ice. User's accuracies were 96% for Water, 100% for Snow, 86% for Melting Snow, and 78% for Ice.

On 28 May, the classification achieved an overall accuracy of 89% (±2%). Only Water and Snow classes were detected. Producer's accuracies were 100% for Water and Snow. User's accuracies were 82% for Water and 94% for Snow.

Zoomed view of Panguingue Creek

The spatial analysis shows that rivers with a width of less than 20 m are not consistently classified as open water by the algorithm (Figure 23). However, these same segments are classified as ice or snow when those surface conditions are present. This pattern holds true across several stream sections within the study area. Sections above 30 m in width are more reliably classified.

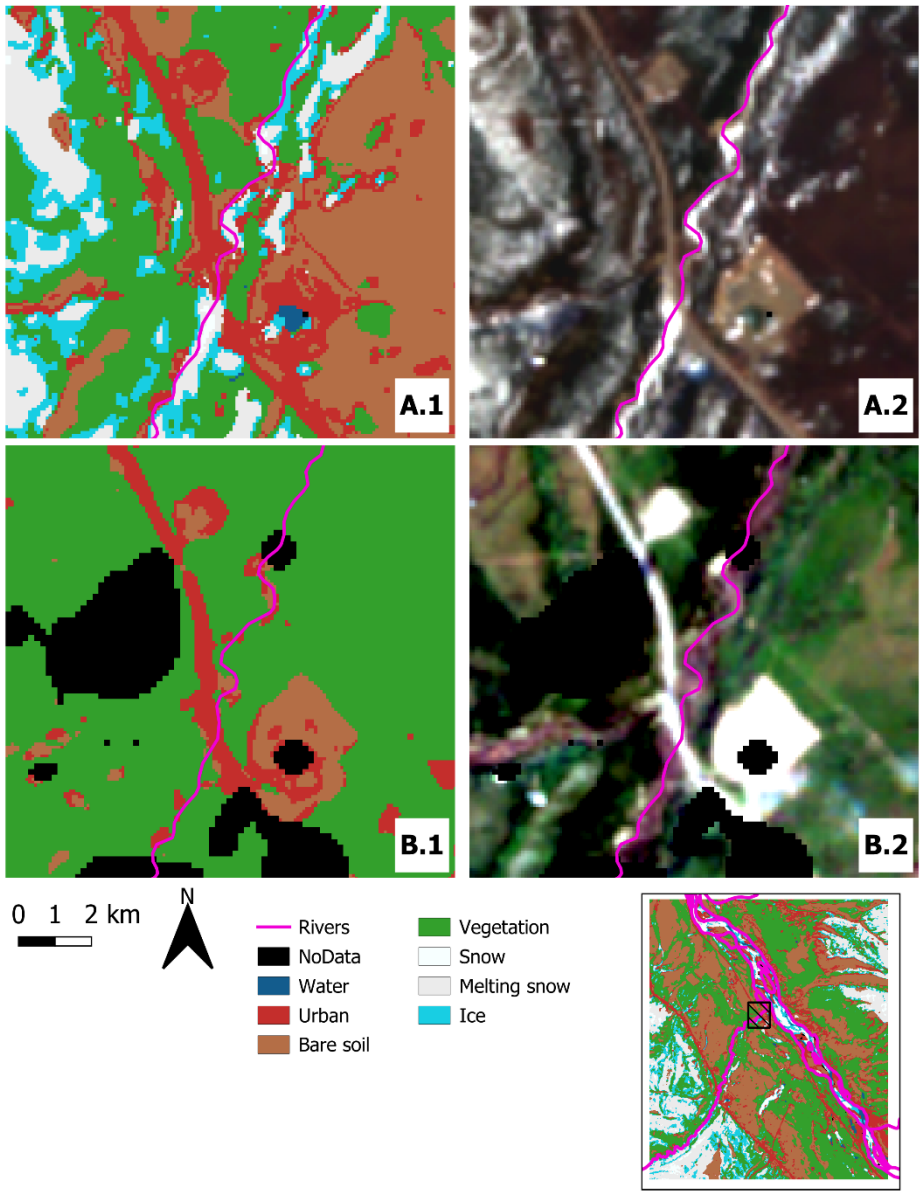


Figure 23: Targeted analysis of two areas within the Panguingue Creek ROI to qualitatively assess river detection, with indicative river presence provided to support visual interpretation. Images A were acquired on 05 May, and images B on 28 May. (A.1, B.1) Random Forest classification from Sentinel-2; (A.2, B.2) Sentinel-2 imagery. (Source: Sentinel-2, Copernicus Browser; Gerad Smith).

Zoomed view of Nenana

For the Nenana ROI, the consistency of the river detection remains the same as for the Panguingue Creek ROI. This pattern holds true across several stream sections within the study area.

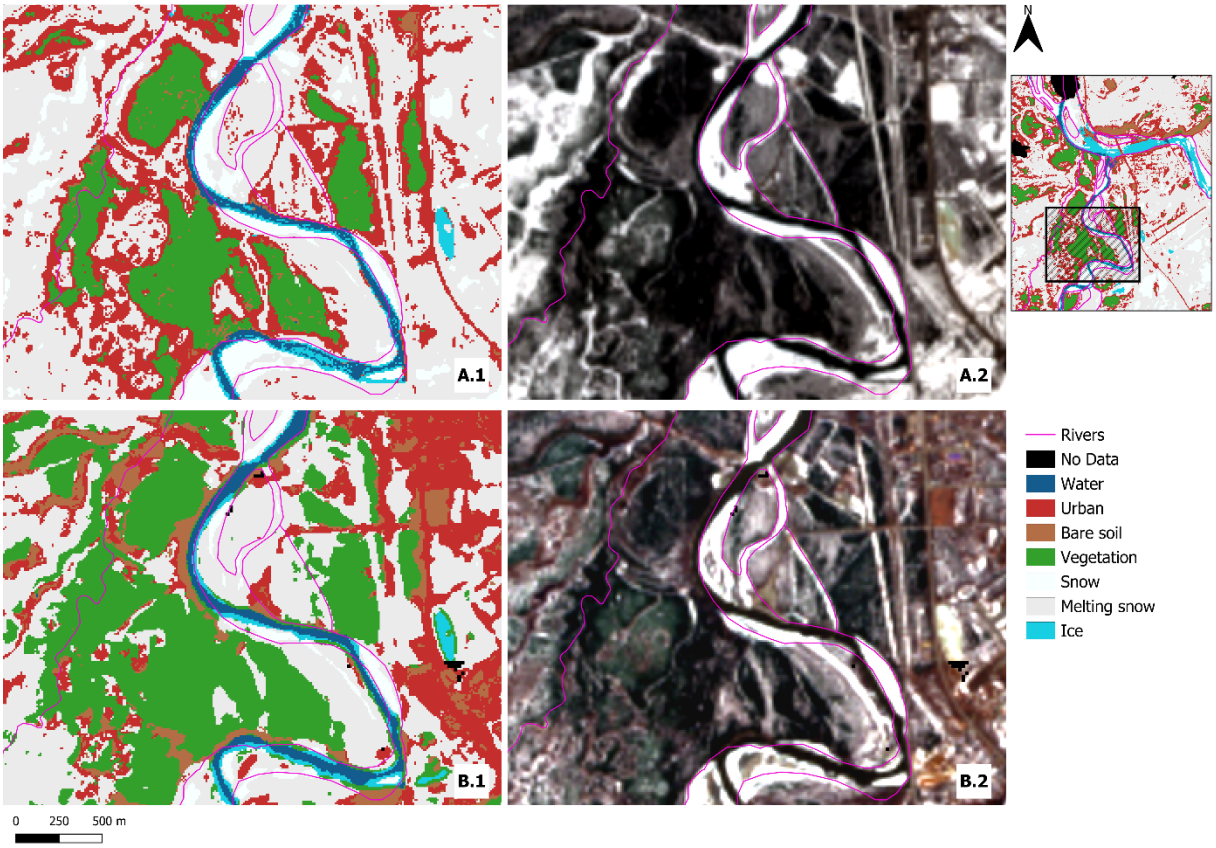


Figure 24: Targeted analysis of two areas within the Nenana ROI qualitatively assess river detection, with indicative river presence provided to support visual interpretation. Images A were acquired on 25 April, and images B on 05 May. (A.1, B.1) Random Forest classification from Sentinel-2; (A.2, B.2) Sentinel-2 imagery. (Source: Sentinel-2, Copernicus Browser; Gerad Smith).

6.2.2. Visual analysis

Several Sentinel-2 and PlanetScope images, initially excluded due to partial cloud cover filtering, were re-examined visually. While unsuitable for automated classification, these images provide sufficient quality to visually identify indicators of river ice breakup, such as changes in texture, reflectance, or the presence of an ice-free channel. This qualitative analysis allowed, in some cases, a reduction of the uncertainty window. For Panguingue Creek, PlanetScope imagery narrowed this window to the period between 8 and 13 May, while Sentinel-2 imagery limited it between 8 and 15 May. For Nenana, cloud cover around the breakup (1 May) doesn't allow a reduction of the uncertainty window.

6.2.3. SAR analysis – Sentinel-1

To analyse the spatial resolution objective through sentinel-1 data, time series of backscatter difference were created. Two types of differences were used: absolute difference or relative difference in backscatter values. Results are presented first for the Nenana ROI, then for the Panguingue Creek ROI.

For the Nenana ROI, absolute and relative differences in Sentinel-1 backscattering gives mixed results. Overall, there is a clear signal for river ice cover change (Figure 25). However, there is no robust signal for rivers width smaller than 50 meters.

Difference in river cover are more pronounced first for the Nenana River and its junction with the Tanana River (Figure 25A.2, B.2). The difference after the breakup, between the 18 and 6 May highlights more changes in the Tanana River (Figure 25C.2).

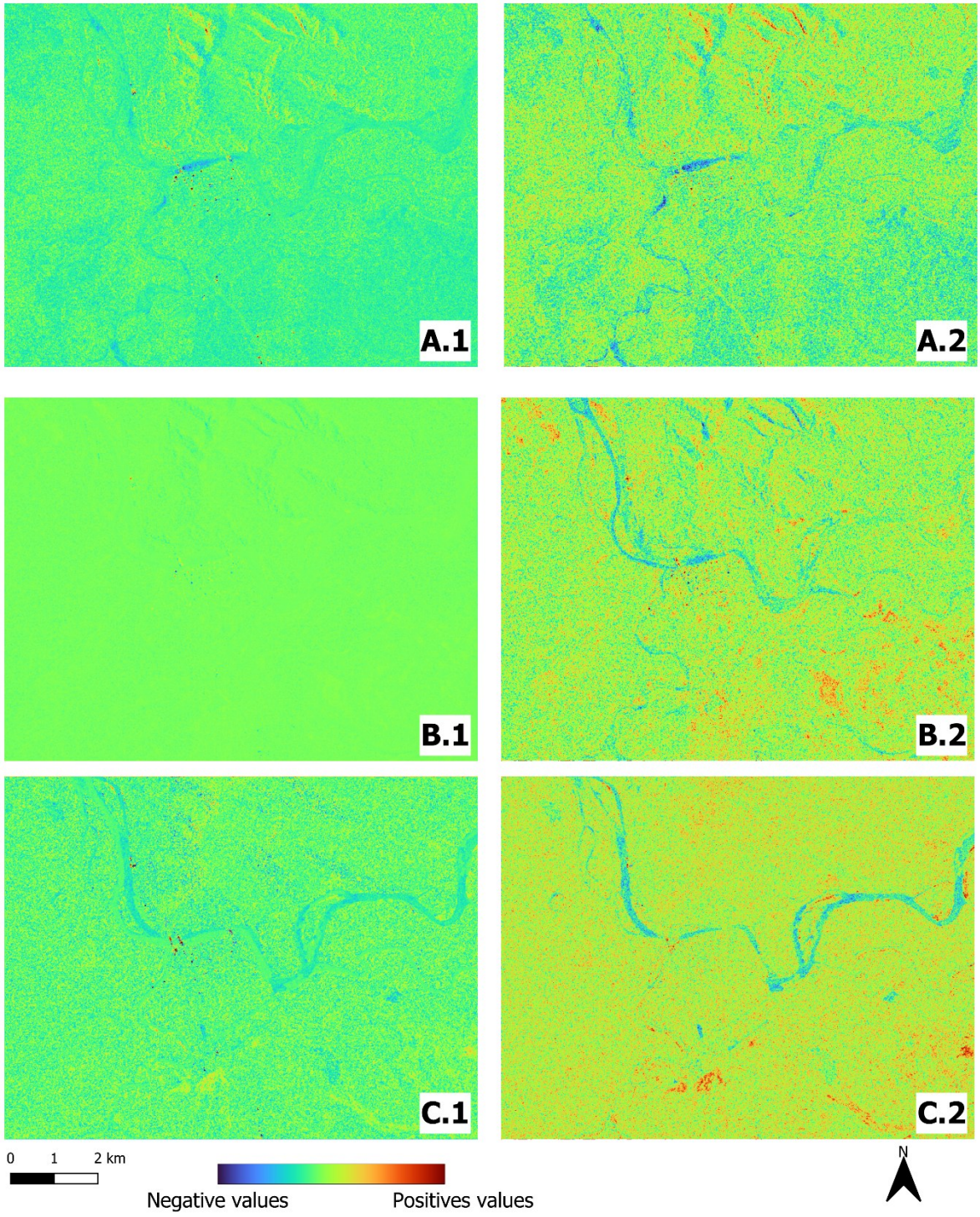


Figure 25: Absolute and relative differences in Sentinel-1 backscattering between three sets of dates at the Nenana ROI. A) 24-22 April B) 4 May-24 April C) 18-6 May. (A.1, B.1, C.1) Absolute difference in backscattering; (A.2, B.2, C.2) Relative difference in backscattering. Maximum and minimum values differ slightly for each date; therefore, no units were added in the legend. (Source: Sentinel-1 GRD IW VV band, Copernicus Browser).

For Panguingue Creek, absolute difference yields more contrasted results than relative difference (Figure 26). Even if the stream of Panguingue Creek can be discerned, the signal remains rough. The overall “salt and pepper effect” makes it difficult to draw accurate conclusions about river size detection.

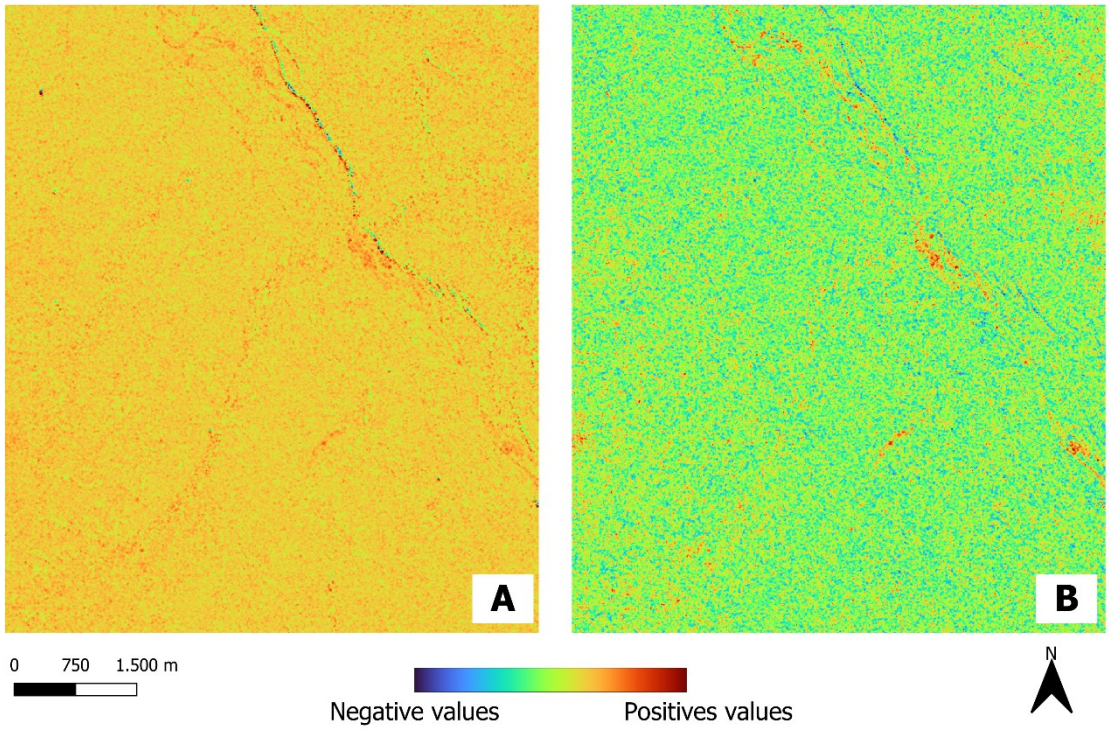


Figure 26: Absolute and relative differences in Sentinel-1 backscattering between 18 May and 06 May at the Panguingue Creek ROI. A) Absolute difference; B) Relative difference. Maximum and minimum values differ slightly for each date; therefore, no units were added in the legend. (Source: Sentinel-1 GRD IW VV band, Copernicus Browser).

7. Discussion

7.1. How the temporal resolution of satellite observation affects the detection of river ice breakup

Breakup was examined across several rivers of varying sizes to evaluate potential differences in breakup timing, following river junction from the Yukon River to small tributaries such as Panguingue Creek. The working hypothesis related to the first sub-objective suggesting that smaller rivers undergo earlier breakup due to lower thermal inertia could not be verified, due to several limiting factors.

We assessed the temporal resolution of open access satellite imagery in detecting river ice breakup. To that end, we examined the revisit frequency and data reliability of Sentinel-1 and Sentinel-2. Although Sentinel-2 is expected to acquire imagery at intervals shorter than five days at these latitudes, cloud cover often obstructed optical observation (J. Li & Chen, 2020). Additionally, data were frequently unavailable on the Copernicus Browser. Both these factors limited Sentinel-2 data's availability.

Sentinel-1 provides radar imagery unaffected by cloud cover; however, it presents its own challenges. Signal inconsistencies exist between ascending and descending swaths due to varying incidence angles (Schaufler et al., 2018a). The possibility of combining swaths through additional preprocessing to increase temporal coverage was considered, though risks of introducing inconsistencies were judged too high for dynamic conditions in small river systems (Schaufler et al., 2018b; Yan et al., 2022). Consequently, this study used only one swath direction (ascending) to avoid signal interference, effectively reducing the revisit frequency to 12 days. However, due to overlap between swaths from adjacent orbits, the revisit frequency increased with different viewing conditions. This proved useful for Sentinel-1, reducing the revisit time of 12 days to two or 10 days (Figure 19).

These gaps limit the utility of Sentinel-1 and Sentinel-2 for precisely pinpointing breakup dates, but help reducing their uncertainty window. When used individually, they respectively help reducing the breakup time window to 12 and 23 days for Panguingue Creek, and 12 and 10 days for Nenana (Figure 19). When Sentinel data is combined together, the window is further reduced by two days for the breakup in Nenana, leading to a 10 day uncertainty window. The combining method doesn't improve the time window for Panguingue Creek, leaving it at best at a 10 days uncertainty window. The Tanana ROI, located between two Sentinel swath, has very poor coverage resulting in an uncertainty window of at best 24 days, judged too big to be of any help. Planet imagery, with near daily revisit time, could help reduce the uncertainty window but limitations regarding inconsistent radiometry, frequent image blur, and geolocation errors hinder accurate detection (Frazier & Hemingway, 2021; Kim et al., 2021). Therefore, it was only used for validation purposes.

The retrieved break-up dates seem to contradict the hypothesis of earlier breakup on smaller rivers due to thermal inertia in a calendar year sense. For the same year (2018), ice breakup is happening first for the Tanana River in Nenana (1 May), then six days later for the largest river, the Yukon River at Tanana (7 May), and lastly four more days later at the smallest river, Panguingue Creek (10 May). However, if "earlier" means the timing relative to when mean air temperature first rises above 0 °C, the hypothesis is verified for 2018. Indeed, at the Panguingue Creek, Nenana, and Tanana ROIs, daily mean air temperatures exceed 0 °respectively 6, 8, and 12 days before the breakup (river size is smallest at the Panguingue Creek ROI, and biggest at the Tanana ROI).

Varying observational methods introduce uncertainties in breakup dating, complicating direct comparisons across regions (Prowse et al., 2007). Breakup dates should therefore be compared with caution, and generalization should be avoided as it's only based on a year worth of data. Nonetheless, all study sites are located within a 150 km radius in central Alaska, a region unaffected by maritime or southern mountain influences on climate patterns (Alaska Climate Research Center, n.d.-a). Therefore, observed differences in breakup timing seem to more likely reflect local factors, such as channel morphology and topography, who in turn influences air temperature, rather than broader climactic patterns (Lind et al., 2016; Thellman et al., 2021).

7.2. Minimum river width for which ice breakup can be reliably detected based on the spatial resolution analysis

The spatial resolution component investigated how river ice, snow, and open water could be accurately differentiated using satellite imagery, and until which resolution. The working hypothesis related to the second sub-objective is based on a general remote sensing principle: to reliably detect a feature, it must be at least twice the size of the sensor's spatial resolution. Thus, narrower rivers may fall below the detectable threshold for high-resolution sensors like Sentinel-1 and Sentinel-2.

7.2.1. Sentinel-2 Random Forest classification

Sentinel-2 RF classification offered varying results depending on the date and the ROI. In the Panguingue Creek ROI, differences emerged if river ice was thawed or not. On 5 May, ice cover on Panguingue Creek was detected from widths of 13 m, while on 28 May, when the Panguingue Creek stream was now open water, it wasn't detected at all (Figure 23). Vegetation along the banks may have obscured the spectral signal, and increased sediment load following breakup can darken the water, shifting its reflectance toward that of bare soil or vegetation (e.g., Herrault et al., 2016). In the Nenana ROI, both ice and open water sections of at least 13 m width became discernible on 5 May and again on 28 May (Figure 24). For both ROIs, classification robustness increased vastly for channel widths of 20-30 m and above. Similar results were found by D. Li et al. (2020): open water rivers with width over 30 m could be well extracted and connected together.

This finding challenges the rule of thumb that a feature must span at least two pixels for reliable detection, since channels as narrow as 10 to 15 m were occasionally classifiable. However, caution must be applied as there was discrepancy between dates and ROIs.

Classification accuracy was evaluated using confusion matrices, showing that class separability varied significantly. For Panguingue Creek ROI, overall map accuracy oscillates between 71 % and 88 % across the four dates, peaking on 28 May (Table 5). Snow is consistently the best represented class, with producer's accuracy never falling below 87 % and user's accuracy reaching 100 % on 5 May. Melting snow also shows strong map reliability (user's accuracy ≥ 98 %), although its detection steadily weakens over time, with producer's accuracy declining from 79 % on 16 Apr to 58 % on 5 May. As times passed, the amount of melting snow reduced, therefore its signal being more impacted by what's underneath. It could explain this diminution in accuracy. Water classification is more variable: after a strong performance on 25 Apr (PA = 93 %, UA = 68 %), producer's accuracy drops again to 66 % by 28 May, even as user's accuracy temporarily attains 100 %. There are changes in river colour occurring during breakup, driven by sediment and particulate matter inputs. They may have affected detection accuracy by causing misclassification as bare soil. Ice is perfectly captured at the earliest date (PA = 100 %), but its map reliability collapses by 5 May (UA = 14 %) before ice disappears altogether in the final survey.

For Nenana ROI, overall accuracy similarly improves through the season, rising from 79 % on 16 Apr to 89 % on 28 May, reflecting progressive thaw and simpler scene composition (Error! Reference source not found.). Water classification is generally excellent in terms of omission error (PA ≥ 76 %) but exhibits one abnormally low user's accuracy of 6 % on 16 Apr, indicating commission problems in the earliest image; by 5 May water UA recovers to 96 %. Snow producer's accuracy declines sharply mid-season, from 75 % on 16 Apr to 42 % on 5 May, even as user's accuracy remains near perfect, indicating under-detection of snow but few false positives. Melting snow maintains both PA and UA above 83 % at all times, whereas ice shows moderate omission errors early (PA = 72 % on 16 Apr) that improve by 5 May (PA = 100 %), even though user's accuracy never exceeds 82 %. Ice, like at Panguingue Creek, is absent by the final date.

Across both sites, melting snow stands out for its consistently high user's accuracies (> 86 %), meaning that when the map flags melting snow it is almost always correct. Both ROIs lose the ice class by late May, simplifying the classification task and coinciding with the season's highest overall accuracies. In contrast, water accuracy exhibits more temporal volatility, particularly in early April, pointing to spectral confusion with ice or wet soil that diminishes as thaw progresses. Snow omission errors (producer's accuracy) tend to increase midseason at both locations, suggesting that partial snow cover is more challenging to detect than either fully frozen or fully melted surfaces. Overall, both datasets reflect the known challenges of classifying transitional ice, snow and water surfaces using Sentinel2 optical data, especially in small rivers where mixed pixels and rapid surface change undermine classification clarity.

7.2.2. Sentinel-1 backscatter difference

Although advertised as having 10 m resolution, Sentinel-1 actually provides a native spatial resolution of 20 m, which limits the detection of narrow river channels. The adopted workflow utilises VV polarisation GRD backscatter without additional speckle filtering or radiometric refinement. A pronounced decrease in VV polarization backscatter marks ice breakup, as rough ice surfaces transition to smooth open water. VV polarization effectively captures changes in surface roughness, while VH polarization exhibits a lower signal-to-noise ratio for water detection. Although this minimal processing streamlines the methodology, it underperforms relative to what Saal (2023) achieved, detecting ice on a 15 to 50 m width river with 73% accuracy, reporting clearer ice signatures and higher classification accuracy. Indeed, river features at sub-50 m scales aren't discriminated by our approach (Figure 25; Figure 26).

Both absolute and relative backscatter differencing methods underwent evaluation. The Alaska Satellite Facility (2025) processing guidelines recommend dB scaling for water thresholding, since open water appears darker than surrounding terrain in dB units. However, depending on the ROI, this has not been proven true: relative differencing (dB) yielded stronger signals at the Nenana site, whereas absolute differences produced more distinct signals at Panguingue Creek (Figure 25; Figure 26). These sites specific results seem to indicate that the optimal choice of backscatter metric depends on local environmental conditions.

7.3. Cross-combination of data from satellite imagery with field observations for in situ validation of ice breakup difficult due to data scarcity

To help reduce the ice breakup temporal resolution uncertainty window, a combined approach of satellite imagery and *in situ* data was devised. Ice breakup is a complex matter, so several variables were collected, and a working hypothesis was formulated related to the third sub-objective: river discharge increases immediately after breakup, primarily due to enhanced runoff from melting ice and snow. This pattern has been observed in larger rivers such as the Lena River (the second biggest Arctic river) and may be applied more broadly across Arctic rivers.

The combined approach was not very successful. The use of additional auxiliary datasets, such as air temperature, modelled discharge, and ice thickness could further refine breakup timing, yet their utility is conditional on data availability and spatial alignment with imagery.

Many gauges remain active only during open water seasons or lie downstream of incomplete ice cover, limiting their relevance for direct breakup detection. Instruments to measure ice thickness or subsurface flow remain limited in winter mainly due to technical, logistical, and environmental challenges. Thick snow cover and low temperatures make *in situ* measurements difficult, costly, and hazardous. Satellite and remote sensing techniques also struggle: for example, radar and lidar signals can be distorted or absorbed by overlying snow, and it is often hard to determine the interface between snow, ice, and water (Lakshminarayanan & Sriraam,

2014; Thellman et al., 2021; Richards et al., 2023). Furthermore, satellite-based discharge models currently apply only to open water season, in the summer (Bjerklie et al., 2018).

Only the Nenana ROI had discharge data during breakup, and it was estimated (Figure 20). The hypothesis that river discharge peaks immediately after ice breakup, observed in large basins such as the Lena River, does not consistently apply to smaller systems. Estimated flow records for the Nenana ROI exhibit a lag between breakup and peak discharge of 12 days (Figure 20). However, even if verified by an USGS expert, the Nenana ROI data remains estimated, so peak discharge could be happening at another moment. A possible explanation to this delay could be due to the type of breakup happening: a mechanical breakup results in a higher and more sudden spike discharge than a thermal breakup (Beltaos & Prowse, 2009; Thellman et al., 2021). Mechanical breakups are often associated with intense runoff and heavy precipitation before ice melting (Thellman et al., 2021). Aside from the fact that it is in a different location, a large river basin in the case of the Lena River could collect more runoff than the Tanana River at Nenana, therefore heightening the chance of mechanical breakup occurring.

A comparison with the year 2009 could be made, where an extreme case of mechanical breakup caused historic floods all around Alaska, for example raising the water level by 9 m in 48h in Eagle (Lindsey, 2019). In 2009, peak discharge is occurring on May 5, 4 days after breakup (Figure 27). It is an eight days difference compared to 2018. Peak discharge is also higher in 2009 than in 2018, respectively reaching 1,830 m^3/s and 1,460 m^3/s. Those differences seem to highlight the importance of the type of breakup for earlier peak discharge dates, 2009 being a mechanical one and 2018 being more thermal one. As mean discharge data still is partially estimated by the USGS, caution remains advised regarding those interpretations (USGS, 2019, 2024).

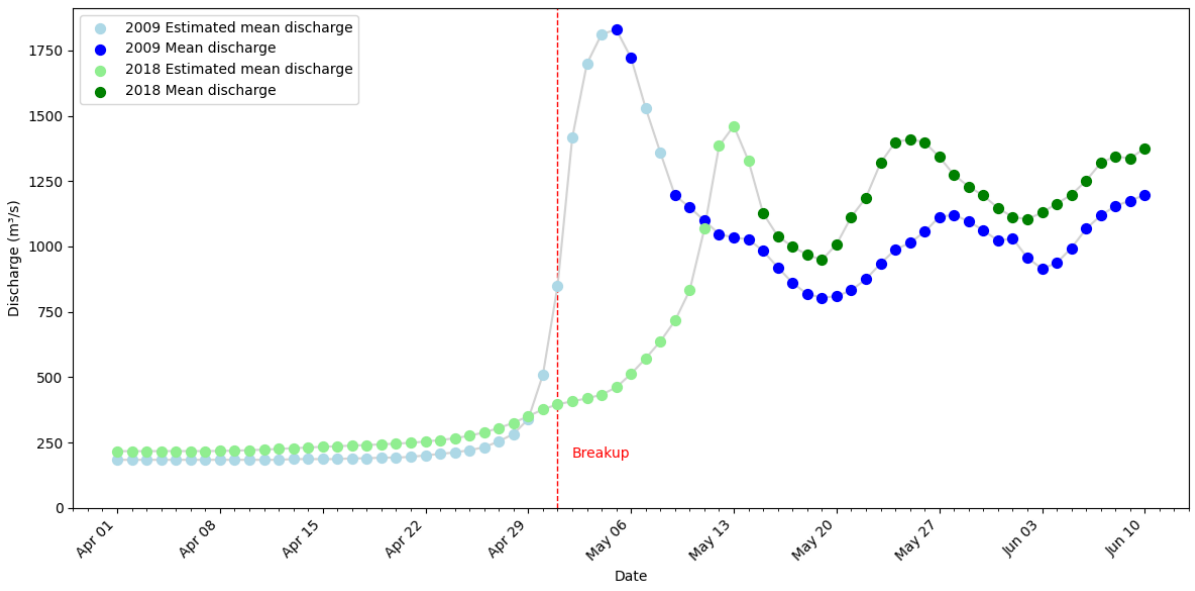


Figure 27: Comparison of mean river discharge (m^3/s) of the Tanana River at the Nenana ROI in 2009 and 2018. Mean discharge is directly measured from station USGS-15515500 data. Estimated mean

discharge is based on expert judgement (USGS, 2019, 2024). Coincidentally, breakup is occurring on the same day, May 1. (Sources: NOAA, n.d.; USGS, n.d.).

Ice thickness measurements were only found for the Nenana ROI; 63.5 cm thick on April 18, or 61% of the historical ice thickness average for the month of April (Nenana Ice Classic, 2018; NOAA, n.d.-b). The nearest available measurements to the ROIs are from Fairbanks, and reached in April 2018 28 inches (71 cm), representing 108% of the historical average (NOAA, n.d.-b). With Fairbanks being located only 75 km east of the Nenana ROI, it shows that this distance is sufficient to vastly impact ice thickness. Therefore, approximating this value to the other ROIs wasn't judged viable. Lower ice thickness can reduce the risk of mechanical breakup, resulting in less ice jams, therefore impacting peak river discharge (Lindsey, 2019; Thellman et al., 2021). In April 2009, ice thickness measured in the Nenana ROI was equal to 45 inches (114 cm), or 110% of of the historical average (NOAA, n.d.-b). Even tough ice thickness doesn't solely influence both the timing and intensity of river ice breakup, the difference between 2009 and 2018 seem to corroborate the fact that different types of breakup occurred in both years, impacting peak discharge (Lindsey, 2019).

Thermal inertia influences breakup timing but does not solely determine it (Thellman et al., 2021). At Panguingue Creek, Nenana, and Tanana, air temperatures exceeded 0 °C several days before breakup, yet the observed event dates varied by more than a week (Figure 20). These discrepancies seem to suggest that river morphology, ice thickness, and heat exchange dynamics all play significant roles in breakup timing.

7.4. Methodological uncertainties and limitations

Changing conditions during breakup reduced the ability to generate time series composites, limiting data robustness. Rapid land cover changes within days also prevented effective integration of Sentinel-1 and Sentinel-2 imagery together, as acquisition dates rarely aligned.

7.4.1. Sentinel-2 Random Forest classification

Cloud screening

The cloud screening with the resampled SCL used to filter clouds, cloud shadows, and other unwanted classes, wasn't foolproof (Figure 28). While the cloud in itself was successfully removed, its shadow wasn't, leading to unwanted pixels being erroneously accorded to several classes. While a minority, repeated errors impacted negatively the overall accuracy of the classifications.

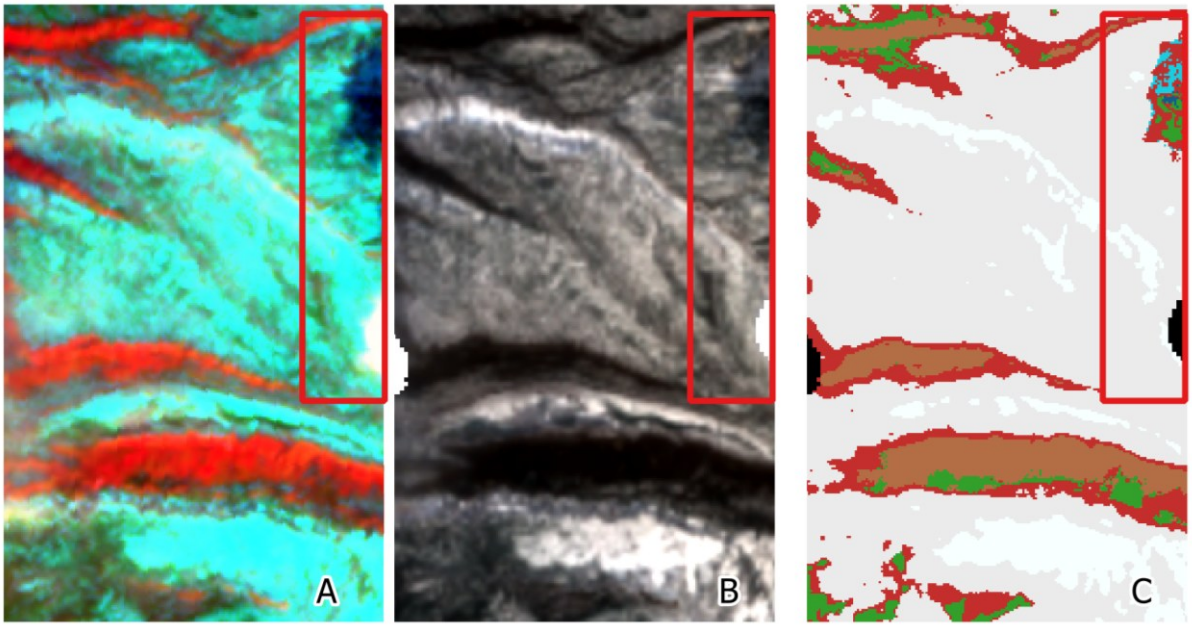


Figure 28: Exemples of errors in the cloud screening preprocessing for the Panguingue Creek ROI on April 25. A) SWIR; B) True Color; C) RF classification.

Validation

Empirical indices (NDSI, NDWI) proved unreliable for consistent discrimination, whereas synthetic SWIR composites and false colour combinations NDVI improved ice versus snow separation.

We implemented Random Forest via the Dzetsaka plugin in QGIS and validated results with the AcATaMa plugin, employing stratified random sampling with 50 samples per class as recommended per Stehman & Foody (2019). As these are separate plugins, there is a possibility that validation samples were taken from training polygons, possibly inflating accuracy estimates. Expanding to 100 samples per class could reduce this bias.

Visual validation encountered further challenges. Variations in snow hue and reflectance altered scene tone without changing pixel values, complicating manual inspection.

7.4.2. Sentinel-1 backscatter differences

Further processing of Sentinel-1 data could have improved image co-registration and reduced geometry mismatch, enabling analysis at shorter temporal intervals, particularly for the Panguingue Creek ROI. The available dataset for the Nenana ROI would barely change, with only the 28 May image being added back. Further processing would also allow comparison with studies using sigma naught backscatter, improving ice, snow, and water discrimination (Surdu et al., 2015). Incorporating quantification might provide additional proxies to assess the timing and progression of river ice breakup.

8. Conclusion

This study set out to improve detection of ice breakup in small Arctic rivers using open-access satellite imagery and *in situ* data. The main objective was to determine what is the minimum river size where ice break-up is detectable in the Arctic using open access satellite imagery. The analysis combined Sentinel-1 SAR backscatter differencing, Sentinel-2 Random Forest classifications, and high-resolution PlanetScope reference imagery, with *in situ* measurements. The study focussed on three ROIs covering a range of Arctic rivers of varying sizes in central Alaska, near Healy, Nenana and Tanana, were selected. This enabled the evaluation of classification methods' performance across different spatial scales, including river junctions and narrow channels. Due to exceptional breakup coverage from Opfergelt et al. on the smallest river Panguingue Creek, the analysis centred around the 2018 breakup season (April-May).

The first objective evaluated how observation frequency affects the timing accuracy of breakup detection. The working hypothesis proposed that smaller rivers break up earlier due to lower thermal inertia. The hypothesis seems to be supported by the 2018 observations. On one hand, satellite data reduced the temporal uncertainty window but couldn't reveal a consistent pattern of earlier breakup on smaller channels. Ice breakup detection windows varied by site and satellite, from about 10 to 39 days. Combining Sentinel-1 and Sentinel-2 imagery reduced this window from 12 to 10 days for the Nenana ROI. Cloud cover, revisit time, geometry mismatch, and gaps in the archive limited temporal precision. On the other hand, average daily air temperatures consistently exceed 0 °C several days prior to the observed breakup at the Panguingue Creek, Nenana, and Tanana ROIs. This occurs 6, 8, and 12 days in advance, respectively, which seems to corroborate the fact that smaller rivers breakup does happen earlier. Here, "earlier" doesn't refer to calendar dates but to the timing relative to when mean air temperature first rises above 0 °C. Caution is advised as the hypothesis is only verified on a year's worth of data.

The second objective assessed spatial resolution limits and aimed to define the minimum detectable river width. The expectation that a feature must exceed the sensor resolution by a twofold margin proved broadly valid. Sentinel-2 optical classifications produced reliable, repeatable detection for channels roughly 20 to 30 m wide and above. Occasional correct classifications occurred for reaches of 10 to 15 m, but these were inconsistent across dates and sites. Under the minimally processed workflow, Sentinel-1 backscatter differencing yielded robust signals only for channels of about 50 m or wider. Thus, practical detection thresholds in the studied conditions were approximately 20 to 30 m for Sentinel-2 and around 50 m for Sentinel-1.

The third objective tested whether combining satellite and field data improves breakup interpretation. The working hypothesis expected an immediate post-breakup rise in discharge due to melt and runoff. This pattern did not hold consistently at the study sites. In the Nenana ROI, the 2018 peak discharge occurred approximately 12 days after breakup, indicating a lag rather than an immediate spike. A comparison with 2009, where historic mechanical breakups

happened across Alaska, showed a larger peak about eight days earlier, reaching 1,830 m^3/s in 2009 *versus* 1,460 m^3/s in 2018. This seems to suggest that breakup type strongly influences the timing and magnitude of flow response. Sparse *in situ* records of river discharge and ice thickness limited the analysis to the Nenana ROI.

Future research could investigate alternative proxies, such as river colour changes due to sediment load following breakup. These variations, observable in optical imagery, might indicate breakup more precisely if consistently correlated with surface conditions.

In situ discharge, water temperature, and ice thickness measurements are difficult to obtain during frozen conditions, but they can critically validate satellite-based estimates. Few studies document river ice thickness or subsurface flow, and most discharge records begin only after ice breakup. Expanding ground-based monitoring networks or deploying autonomous sensors would bridge this data gap and support robust remote sensing validation.

Bibliography

AcATaMa. (n.d.). AcATaMa. Retrieved June 8, 2025, from https://smbyc.github.io/AcATaMa/

Adam, E., Mutanga, O., Odindi, J., & Abdel-Rahman, E. M. (2014). Land-use/cover classification in a heterogeneous coastal landscape using RapidEye imagery: Evaluating the performance of random forest and support vector machines classifiers. *International Journal of Remote Sensing*, *35*(10), 3440–3458. https://doi.org/10.1080/01431161.2014.903435

Adrian, R., O'Reilly, C. M., Zagarese, H., Baines, S. B., Hessen, D. O., Keller, W., Livingstone, D. M., Sommaruga, R., Straile, D., Van Donk, E., Weyhenmeyer, G. A., & Winder, M. (2009). Lakes as sentinels of climate change. *Limnology and Oceanography*, *54*(6part2), 2283–2297. https://doi.org/10.4319/lo.2009.54.6_part_2.2283

Agrawal, S., & Khairnar, G. B. (2019). A COMPARATIVE ASSESSMENT OF REMOTE SENSING IMAGING TECHNIQUES: OPTICAL, SAR AND LIDAR. *The International Archives of the Photogrammetry, Remote Sensing and Spatial Information Sciences*, *XLII-5-W3*, 1–6. ISPRS WG V/7 & WG IV/6
International Workshop on "Capacity Building and Education Outreach in Advanced Geospatial Technologies and Land Management" (Volume XLII-5/W3) - 10–11 December 2019, Dhulikhel, Nepal. https://doi.org/10.5194/isprs-archives-XLII-5-W3-1-2019

Alaska Climate Research Center. (n.d.-a). *Climate – Alaska Climate Research Center*. Retrieved July 7, 2025, from https://akclimate.org/climate/

Alaska Climate Research Center. (n.d.-b). *Climate Change in Alaska – Alaska Climate Research Center*. Retrieved July 7, 2025, from https://akclimate.org/climate-change-in-alaska/

Alaska Satellite Facility. (2025). *Introduction to SAR - HyP3*. https://hyp3-docs.asf.alaska.edu/guides/introduction_to_sar/

AMAP. (2021). *Arctic Climate Change Update 2021: Key Trends and Impacts. Summary for Policy-makers | AMAP*. https://www.amap.no/documents/doc/arctic-climate-change-update-2021-key-trends-and-impacts.-summary-for-policy-makers/3508

Beltaos, S., & Burrell, B. C. (2003). Climatic change and river ice breakup. *Canadian Journal of Civil Engineering*, *30*(1), 145–155. https://doi.org/10.1139/l02-042

Beltaos, S., & Prowse, T. (2009). River-ice hydrology in a shrinking cryosphere. *Hydrological Processes*, *23*(1), 122–144. https://doi.org/10.1002/hyp.7165

Bennett, K. E., & Prowse, T. D. (2010). Northern Hemisphere geography of ice-covered rivers. *Hydrological Processes*, *24*(2), 235–240. https://doi.org/10.1002/hyp.7561

Bjerklie, D. M., Birkett, C. M., Jones, J. W., Carabajal, C., Rover, J. A., Fulton, J. W., & Garambois, P.-A. (2018). Satellite remote sensing estimation of river discharge: Application to the Yukon River Alaska. *Journal of Hydrology*, *561*, 1000–1018. https://doi.org/10.1016/j.jhydrol.2018.04.005

Bouvet, A., Mermoz, S., Ballère, M., Koleck, T., & Le Toan, T. (2018). Use of the SAR Shadowing Effect for Deforestation Detection with Sentinel-1 Time Series. *Remote Sensing*, *10*(8), 1250. https://doi.org/10.3390/rs10081250

Breiman, L. (2001). Random Forests. *Machine Learning*, *45*(1), 5–32. https://doi.org/10.1023/A:1010933404324

Dong, Y., Xiao, P., Zhang, X., Ge, D., Yu, J., Chen, Y., Wu, Q., Ma, Y., Liu, R., Luan, W., Liu, H., & Bai, J. (2025). Increased vulnerability of Arctic potential ice roads under climate change. *Communications Earth & Environment*, *6*(1), 1–9. https://doi.org/10.1038/s43247-025-02011-y

Du, J., Kimball, J. S., Duguay, C., Kim, Y., & Watts, J. D. (2017). Satellite microwave assessment of Northern Hemisphere lake ice phenology from 2002 to 2015. *The Cryosphere*, *11*(1), 47–63. https://doi.org/10.5194/tc-11-47-2017

ESA. (n.d.). *S1 Processing*. Retrieved July 7, 2025, from https://sentiwiki.copernicus.eu/web/s1-processing

ESA. (2025). *S1 Mission*. https://sentiwiki.copernicus.eu/web/s1-mission

Frazier, A. E., & Hemingway, B. L. (2021). A Technical Review of Planet Smallsat Data: Practical Considerations for Processing and Using PlanetScope Imagery. *Remote Sensing*, *13*(19), 3930. https://doi.org/10.3390/rs13193930

Fung, P. L., Zaidan, M. A., Timonen, H., Niemi, J. V., Kousa, A., Kuula, J., Luoma, K., Tarkoma, S., Petäjä, T., Kulmala, M., & Hussein, T. (2021). Evaluation of white-box versus black-box machine learning models in estimating ambient black carbon concentration. *Journal of Aerosol Science*, *152*, 105694. https://doi.org/10.1016/j.jaerosci.2020.105694

Herrault, P.-A., Gandois, L., Gascoin, S., Tananaev, N., Le Dantec, T., & Teisserenc, R. (2016). Using High Spatio-Temporal Optical Remote Sensing to Monitor Dissolved Organic Carbon in the Arctic River Yenisei. *Remote Sensing*, *8*(10), Article 10. https://doi.org/10.3390/rs8100803

IBM Integrated Analytics System. (2022, October 4). https://www.ibm.com/docs/en/ias?topic=procedures-statistics-parametric-nonparametric

IPCC. (2023). *Climate Change 2022 – Impacts, Adaptation and Vulnerability: Working Group II Contribution to the Sixth Assessment Report of the Intergovernmental Panel on Climate Change* (1st ed.). Cambridge University Press. https://doi.org/10.1017/9781009325844

Karasiak, N. (2016). *Dzetsaka* [Python]. https://github.com/nkarasiak/dzetsaka (Original work published 2016)

Kennedy, E., Celis, G., See, C. R., Schaedel, C., Mauritz, M., Taylor, M., Ledman, J., Natali, S., Schuur, E., & Bonanza Creek LTER. (2025). *Eight Mile Lake Research Watershed: Hourly meteorological data, 2004-2024* [Dataset]. Environmental Data Initiative. https://doi.org/10.6073/PASTA/9B3B2F032161B09C4FF6BEC8892BD4B0

Kim, M., Park, S., Anderson, C., & Stensaas, G. L. (2021). System characterization report on Planet's Dove Classic. In *Open-File Report* (Nos. 2021-1030–C). U.S. Geological Survey. https://doi.org/10.3133/ofr20211030C

Kingma, D. P., & Ba, J. (2014). *Adam: A Method for Stochastic Optimization* (Version 9). arXiv. https://doi.org/10.48550/ARXIV.1412.6980

Lakshminarayanan, V., & Sriraam, N. (2014). The effect of temperature on the reliability of electronic components. *2014 IEEE International Conference on Electronics, Computing and Communication Technologies (CONECCT)*, 1–6. https://doi.org/10.1109/CONECCT.2014.6740182

Lary, D. J., Alavi, A. H., Gandomi, A. H., & Walker, A. L. (2016). Machine learning in geosciences and remote sensing. *Geoscience Frontiers*, *7*(1), 3–10. https://doi.org/10.1016/j.gsf.2015.07.003

Lawrence, R. L., & Moran, C. J. (2015). The AmericaView classification methods accuracy comparison project: A rigorous approach for model selection. *Remote Sensing of Environment*, *170*, 115–120. https://doi.org/10.1016/j.rse.2015.09.008

Lee, Joonwhoan. (2014). Extreme Learning Machine Ensemble Using Bagging for Facial Expression Recognition. *Journal of Information Processing Systems*, *10*(3), 443–458. https://doi.org/10.3745/JIPS.02.0004

Lesack, L. F. W., Marsh, P., Hicks, F. E., & Forbes, D. L. (2014). Local spring warming drives earlier river-ice breakup in a large Arctic delta. *Geophysical Research Letters*, *41*(5), 1560–1567. https://doi.org/10.1002/2013GL058761

Li, D., Wu, B., Chen, B., Qin, C., Wang, Y., Zhang, Y., & Xue, Y. (2020). Open-Surface River Extraction Based on Sentinel-2 MSI Imagery and DEM Data: Case Study of the Upper Yellow River. *Remote Sensing*, *12*(17), Article 17. https://doi.org/10.3390/rs12172737

Li, J., & Chen, B. (2020). Global Revisit Interval Analysis of Landsat-8 -9 and Sentinel-2A -2B Data for Terrestrial Monitoring. *Sensors (Basel, Switzerland)*, *20*(22), 6631. https://doi.org/10.3390/s20226631

Lind, L., Alfredsen, K., Kuglerová, L., & Nilsson, C. (2016). Hydrological and thermal controls of ice formation in 25 boreal stream reaches. *Journal of Hydrology*, *540*, 797–811. https://doi.org/10.1016/j.jhydrol.2016.06.053

Lindsey. (2019). *Spring Breakup on the Yukon: What Happens When the Ice Stops (U.S. National Park Service)*. https://www.nps.gov/articles/aps-18-1-9.htm

Lippitt, C. D., Rogan, J., Li, Z., Eastman, J. R., & Jones, T. G. (2008). Mapping Selective Logging in Mixed Deciduous Forest. *Photogrammetric Engineering & Remote Sensing*, *74*(10), 1201–1211. https://doi.org/10.14358/PERS.74.10.1201

Lu, Y., Zhang, Z., & Huang, D. (2020). Glacier Mapping Based on Random Forest Algorithm: A Case Study over the Eastern Pamir. *Water*, *12*(11), 3231. https://doi.org/10.3390/w12113231

Lund, J., Forster, R. R., Deeb, E. J., Liston, G. E., Skiles, S. M., & Marshall, H.-P. (2022). Interpreting Sentinel-1 SAR Backscatter Signals of Snowpack Surface Melt/Freeze, Warming, and Ripening, through Field Measurements and Physically-Based SnowModel. *Remote Sensing*, *14*(16), 4002. https://doi.org/10.3390/rs14164002

Ma, L., Liu, Y., Zhang, X., Ye, Y., Yin, G., & Johnson, B. A. (2019). Deep learning in remote sensing applications: A meta-analysis and review. *ISPRS Journal of Photogrammetry and Remote Sensing*, *152*, 166–177. https://doi.org/10.1016/j.isprsjprs.2019.04.015

Magnuson, J. J., Robertson, D. M., Benson, B. J., Wynne, R. H., Livingstone, D. M., Arai, T., Assel, R. A., Barry, R. G., Card, V., Kuusisto, E., Granin, N. G., Prowse, T. D., Stewart, K. M., & Vuglinski, V. S. (2000). Historical Trends in Lake and River Ice Cover in the Northern Hemisphere. *Science*, *289*(5485), 1743–1746. https://doi.org/10.1126/science.289.5485.1743

Maxwell, A. E., Warner, T. A., & Fang, F. (2018). Implementation of machine-learning classification in remote sensing: An applied review. *International Journal of Remote Sensing*, *39*(9), 2784–2817. https://doi.org/10.1080/01431161.2018.1433343

Montero, D., Aybar, C., Mahecha, M. D., Martinuzzi, F., Söchting, M., & Wieneke, S. (2023). A standardized catalogue of spectral indices to advance the use of remote sensing in Earth system research. *Scientific Data*, *10*(1), 197. https://doi.org/10.1038/s41597-023-02096-0

Morales-Marín, L. A., Sanyal, P. R., Kadowaki, H., Li, Z., Rokaya, P., & Lindenschmidt, K. E. (2019). A hydrological and water temperature modelling framework to simulate the timing of river freeze-up and ice-cover breakup in large-scale catchments. *Environmental Modelling & Software*, *114*, 49–63. https://doi.org/10.1016/j.envsoft.2019.01.009

Mugunthan, J. S., Duguay, C. R., & Zakharova, E. (2023). Machine learning based classification of lake ice and open water from Sentinel-3 SAR altimetry waveforms. *Remote Sensing of Environment*, *299*, 113891. https://doi.org/10.1016/j.rse.2023.113891

NASA. (2021a, May 18). *Remote Sensing | NASA Earthdata* [Data Basics]. Earth Science Data Systems, NASA. https://www.earthdata.nasa.gov/learn/earth-observation-data-basics/remote-sensing

NASA. (2021b, May 18). *Synthetic Aperture Radar (SAR) | NASA Earthdata* [Data Basics]. Earth Science Data Systems, NASA. https://www.earthdata.nasa.gov/learn/earth-observation-data-basics/sar

Nenana Ice Classic. (2018). *2018 Ice Measurements*. Nenana Ice Classic. https://www.nenanaakiceclassic.com/copy-of-2019

NOAA. (n.d.-a). *Break Up Database*. NOAA's National Weather Service. Retrieved June 8, 2025, from https://www.weather.gov/aprfc/breakupDB?site=469

NOAA. (n.d.-b). *Ice Thickness*. NOAA's National Weather Service. Retrieved June 3, 2025, from https://www.weather.gov/aprfc/icethickness

Olofsson, P., Foody, G. M., Herold, M., Stehman, S. V., Woodcock, C. E., & Wulder, M. A. (2014). Good practices for estimating area and assessing accuracy of land change. *Remote Sensing of Environment*, *148*, 42–57. https://doi.org/10.1016/j.rse.2014.02.015

Pal, M. (2005). Random forest classifier for remote sensing classification. *International Journal of Remote Sensing*, *26*(1), 217–222. https://doi.org/10.1080/01431160412331269698

Planet. (2025). *Education and Research Program | Planet | Planet*. https://www.planet.com/industries/education-and-research/

Prowse, T. D., Bonsal, B. R., Duguay, C. R., & Lacroix, M. P. (2007). River-ice break-up/freeze-up: A review of climatic drivers, historical trends and future predictions. *Annals of Glaciology*, *46*, 443–451. https://doi.org/10.3189/172756407782871431

Rantanen, M., Karpechko, A. Y., Lipponen, A., Nordling, K., Hyvärinen, O., Ruosteenoja, K., Vihma, T., & Laaksonen, A. (2022). The Arctic has warmed nearly four times faster than

the globe since 1979. *Communications Earth & Environment*, *3*(1), 1–10. https://doi.org/10.1038/s43247-022-00498-3

Research – WeThaw. (n.d.). Retrieved August 18, 2025, from https://sites.uclouvain.be/wethaw/research/

Richards, E., Stuefer, S., Rangel, R. C., Maio, C., Belz, N., & Daanen, R. (2023). An evaluation of GPR monitoring methods on varying river ice conditions: A case study in Alaska. *Cold Regions Science and Technology*, *210*, 103819. https://doi.org/10.1016/j.coldregions.2023.103819

Rodriguez-Galiano, V. F., Ghimire, B., Rogan, J., Chica-Olmo, M., & Rigol-Sanchez, J. P. (2012). An assessment of the effectiveness of a random forest classifier for land-cover classification. *ISPRS Journal of Photogrammetry and Remote Sensing*, *67*, 93–104. https://doi.org/10.1016/j.isprsjprs.2011.11.002

Rogan, J., Lippitt, C. D., Toledano, J., Sangermano, F., Eastman, J. R., Mastro, V., & Sawyer, A. (2008). Incorporating anthropogenic variables into a species distribution model to map gypsy moth risk. *Ecological Modelling*, *210*(3), 339–350. https://doi.org/10.1016/j.ecolmodel.2007.08.005

Rösch, M., Sonnenschein, R., Buchelt, S., & Ullmann, T. (2022). Comparing PlanetScope and Sentinel-2 Imagery for Mapping Mountain Pines in the Sarntal Alps, Italy. *Remote Sensing*, *14*(13), 3190. https://doi.org/10.3390/rs14133190

Saal. (2023). *Detecting ice on a narrow river using satellite radar remote sensing*. https://scholar.yukonu.ca/ssaal/2023/detecting-ice-on-a-narrow-river-using-satellite-radar-remote-sensing/

Satellite Applications for Geoscience Education. (n.d.). Retrieved June 2, 2025, from https://cimss.ssec.wisc.edu/sage/remote_sensing/lesson3/concepts.html

Schaufler, S., Bauer-Marschallinger, B., Hochstöger, S., & Wagner, W. (2018a). Modelling and correcting azimuthal anisotropy in Sentinel-1 backscatter data. *Remote Sensing Letters*, *9*(8), 799–808. https://doi.org/10.1080/2150704X.2018.1480071

Schaufler, S., Bauer-Marschallinger, B., Hochstöger, S., & Wagner, W. (2018b). Modelling and correcting azimuthal anisotropy in Sentinel-1 backscatter data. *Remote Sensing Letters*, *9*(8), 799–808. https://doi.org/10.1080/2150704X.2018.1480071

Setyawan, E. (n.d.). *Satellite Imagery: Resolution vs. Accuracy*. Retrieved June 2, 2025, from https://www.intermap.com/blog/satellite-imagery-resolution-vs.-accuracy

Sharma, S., Blagrave, K., Magnuson, J. J., O'Reilly, C. M., Oliver, S., Batt, R. D., Magee, M. R., Straile, D., Weyhenmeyer, G. A., Winslow, L., & Woolway, R. I. (2019). Widespread loss of lake ice around the Northern Hemisphere in a warming world. *Nature Climate Change*, *9*(3), 227–231. https://doi.org/10.1038/s41558-018-0393-5

Stehman, S. V., & Foody, G. M. (2019). Key issues in rigorous accuracy assessment of land cover products. *Remote Sensing of Environment*, *231*, 111199. https://doi.org/10.1016/j.rse.2019.05.018

Stonevicius, E., Uselis, G., & Grendaite, D. (2022). Ice Detection with Sentinel-1 SAR Backscatter Threshold in Long Sections of Temperate Climate Rivers. *Remote Sensing*, *14*(7), Article 7. https://doi.org/10.3390/rs14071627

Surdu, C., Duguay, C., Pour, H., & Brown, L. (2015). Ice Freeze-up and Break-up Detection of Shallow Lakes in Northern Alaska with Spaceborne SAR. *Remote Sensing*, *7*(5), 6133–6159. https://doi.org/10.3390/rs70506133

The Ultimate Guide to Random Forest Regression. (2020). Keboola. https://www.keboola.com/blog/random-forest-regression

Thellman, A., Jankowski, K. J., Hayden, B., Yang, X., Dolan, W., Smits, A. P., & O'Sullivan, A. M. (2021). The Ecology of River Ice. *Journal of Geophysical Research: Biogeosciences*, *126*(9), e2021JG006275. https://doi.org/10.1029/2021JG006275

Turcotte, B., & Morse, B. (2013). A global river ice classification model. *Journal of Hydrology*, *507*, 134–148. https://doi.org/10.1016/j.jhydrol.2013.10.032

Turcotte, B., & Morse, B. (2017). The Winter Environmental Continuum of Two Watersheds. *Water*, *9*(5), 337. https://doi.org/10.3390/w9050337

Turcotte, B., Morse, B., & Anctil, F. (2014). Cryologic continuum of a steep watershed: CRYOLOGIC CONTINUUM OF A WATERSHED. *Hydrological Processes*, *28*(3), 809–822. https://doi.org/10.1002/hyp.9629

USGS. (n.d.). *Tanana R at Nenana AK*. Retrieved June 8, 2025, from http://waterdataui-production.wma.chs.usgs.gov/monitoring-location/15515500/

USGS. (2019, March 3). *How Streamflow is Measured | U.S. Geological Survey*. https://www.usgs.gov/special-topics/water-science-school/science/how-streamflow-measured

USGS. (2024, October 31). *Streamgaging Basics | U.S. Geological Survey*. https://www.usgs.gov/mission-areas/water-resources/science/streamgaging-basics

USGS. (2025). *Watershed Boundary Dataset HUC 12s*. https://www.arcgis.com/sharing/rest/content/items/b60aa1d756b245cf9db03a92254af878

Vonk, J. E., Speetjens, N. J., & Poste, A. E. (2023). Small watersheds may play a disproportionate role in arctic land-ocean fluxes. *Nature Communications*, *14*(1), 3442. https://doi.org/10.1038/s41467-023-39209-7

What Is Random Forest? | IBM. (2021, October 20). https://www.ibm.com/think/topics/random-forest

Yan, L., Wang, J., & Shao, D. (2022). Glacier Mass Balance in the Manas River Using Ascending and Descending Pass of Sentinel 1A/1B Data and SRTM DEM. *Remote Sensing*, *14*(6), Article 6. https://doi.org/10.3390/rs14061506

Yang, X., Pavelsky, T., & Allen, G. (2020). The past and future of global river ice. *Nature*, *577*, 69–73. https://doi.org/10.1038/s41586-019-1848-1

Detecting river ice breakup in small Arctic rivers: combining field data with Sentinel-1 and Sentinel-2 satellite imagery

Case study in the Yukon basin, Alaska

Julien EVRARD

Abstract

Over half of the Northern Hemisphere's river network is seasonally ice-covered, draining more than one-third of Earth's landmass. River ice regulates winter hydrology, sediment transport, and habitat conditions for aquatic and riparian ecosystems. Recent decades have seen later ice freeze-up, earlier ice breakup, and a shortening of the ice season by more than two weeks annually. These shifts, driven by climate change and human activity, have significant impacts on ecosystems and communities.

Monitoring river ice breakup is challenging in remote terrain, and smaller rivers remain largely undocumented due to limited ground observations. Remote sensing offers a valuable means of assessing breakup timing and dynamics.

This study determines the minimum river width at which ice breakup can be detected using open-access satellite imagery in Arctic regions. Three regions of interest in central Alaska are analysed using a combination of two approaches: Sentinel-1 backscatter change detection, and Random Forest classifications of Sentinel-2 time series from 2018, supported by high-resolution PlanetScope imagery. Ground observations of air temperature, discharge, ice thickness, and ice breakup serve as complementary data to the satellite analysis.

Smaller rivers appear to break up sooner relative to thaw, with mean air temperatures exceeding 0 °C several days before breakup at all sites. Breakup detection windows with Sentinel-1 and Sentinel-2 varied widely (10 to 39 days), complicating analysis.

Sentinel-2 reliably detected breakup in rivers about 20 to 30 m wide, and Sentinel-1 required widths near 50 m, confirming that features must exceed sensor resolution by roughly a twofold margin.

Breakup type seems to strongly affect discharge response, though limitation *in situ* data quantity heavily restricted analysis. Expanding ground-based monitoring networks would bridge this data gap and support robust remote sensing validation.

UNIVERSITÉ CATHOLIQUE DE LOUVAIN
Faculté des bioingénieurs
Croix du Sud, 2 bte L7.05.01, 1348 Louvain-la-Neuve, Belgique | **www.uclouvain.be/agro**